Bio-inspired cellular structures for ultralight and high-strength materials

Mechanics of mAterials for enGineering and Integrity of Structures - MAGIS Paris
Track of Polymers and Composite materials

2023-2024

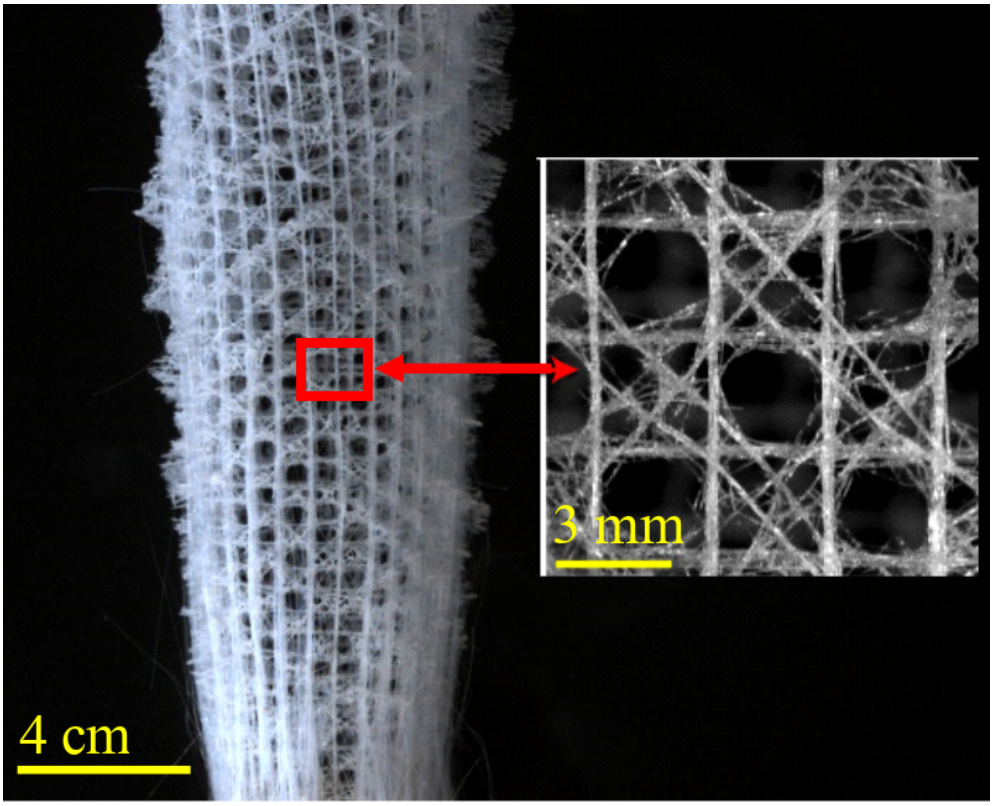

Konstantinos Fotiadis,

Rapporteur : Martin Poncelet

Encadrants :
Lamine Hattali
Laboratoire FAST, Bâtiment Pascal *(bât. 530) Rue André Rivière 91405 Orsay cedex*

Svetlana Terekhina
Laboratoire LAMPA, 2 Bld du Ronceray, BP 93525, 49035 Angers cédex 01

Acknowledgements

I would like to express my sincere gratitude to Mr. Martin Poncelet for accepting to review my report.

From the personel of *Laboratoire FAST,* I would like to thank:

Mr. Amarni Johannes, for his great help in the part of machine optimisation and the preparation of the samples,

Mr. Pauchard Ludovic, for his assistance in the part of microstructure characterization,

Mr. Manquest Christophe, for his assistance with the profilometer machine,

Mr. Aubertin Alban, Mr. Auradou Harold and *Mr. Gargasson Adam*

and *Mr. Caillault Thomas* from the Laboratoire LAMPA, Angers.

Special thanks to Mr. *Beigi Rizi Hassan*, with whom I had the chance to collaborate on this project, for his immense help, guidance and company.

Thanks to all the Doctorate students and the interns of the Laboratoire FAST that made my presence in the lab more enjoyable.

Special thanks to my family and friends for their constant support in this journey and throughout the years.

Finally, I would like to express my immense gratidude to *Mr. Lamine Hattali* who trusted me with this project, guided me and showed me the path to my new passion. Also, *Ms. Svetlana Terekhina* from Laboratoire LAMPA for her collaboration and guidance throughout this project. Their assistance has been instrumental in making this endeavor possible.

Ce mémoire a été réalisé dans le cadre du programme "Bourses de coopération franco-hellénique", qui est mis en œuvre conjointement par la Fondation hellénique de bourses d'études de l'État (I.K.Y.) et le service de coopération et d'action culturelle de l'ambassade de France en Grèce (S.C.A.C.).

Le financement de stage quant à lui a été assuré par l'Objet Interdisciplinaire de l'Institute of Aeronautics and Astronautics OI PSIA2 - RD n°AA-2023-09.

Table of Contents

1. Motivation

Diverse sectors such as civil engineering, automotive, aerospace, and more recently, biomedical field, are actively seeking novel and advanced lightweight, high-performance materials, to meet their demands in energy consumption and for energy absorption applications. The conventional approach used by the engineers, consists of using the lattices structures as a solution. But to this day, engineers stay relatively uninventive when compared to what nature offers us as structures. Nature has always served as a model for mimicking and as inspiration for humans in their desire to improve their lives. By adapting mechanisms and capabilities from nature, scientific approaches have helped humans understand related phenomena and associated principles, in order to engineer novel devices and improve their capability (Bar-Cohen, 2005). Although it only represents a 4% of total numbers of publications, biomimetics and bio-inspired materials, combined with the additive manufacturing technique, on many criteria, could be a possible solution to reduce the energy consumption and improve the mechanical performance (Figure 1). Biomimicry helps to provide relevant designs and concepts with efficient use of materials, while 3D printing is the technological bricks that make them possible.

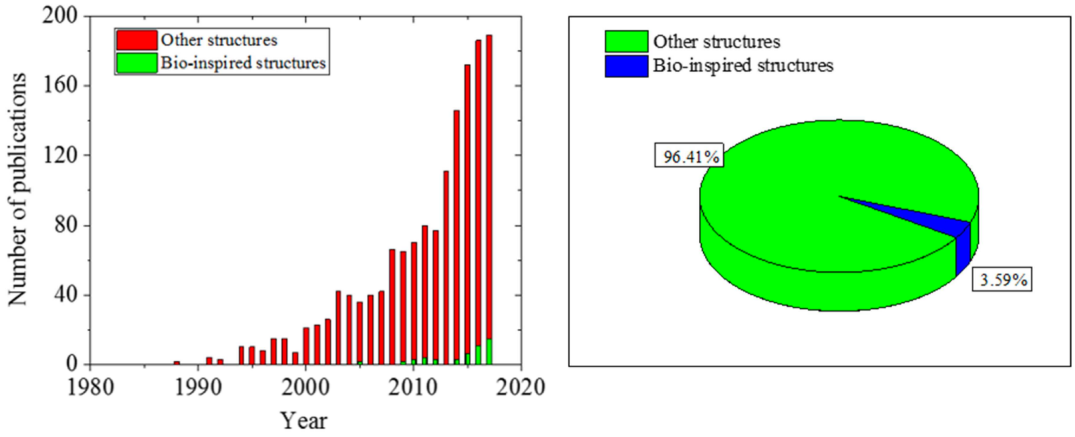

Figure 1: Number of publications of bio-inspired structures for energy absorption based on the Scopus database (Ha and Lu, 2020

In this study, I focus on exploring a biologically inspired structure of the glassy skeletal system from the hexactinellid sponge, Euplectella Aspergillum (EA) through a multi-scale scientific approach (see Figure 2, more details §2.5.2). The motivation to study EA sponge lies in its unique and highly efficient skeletal multi-scale structure. Researchers are interested in this sponge for several reasons: (i) The skeletal system provides insights into biomimetic design, inspiring the creation of new materials and structures that mimic its mechanical efficiency, (ii) offers exceptional buckling resistance, which is valuable for engineering applications requiring lightweight yet strong materials, and (iii) The sponge's ridge design effectively suppresses vortex shedding, which has potential benefits in reducing drag and lift fluctuations in engineering structures exposed to fluid flow. All these advantages have led us to take an interest in studying it as a model structure, drawing inspiration from its architecture. To this end, we have attempted first to study the physico-chemical and mechanical properties of real spicules (the silica that make up the sponge) (Figure 2c), and secondly, replicate the unique square grid design (Figure 2b) using two lightweight brittle materials: (i) Alumina, and (ii) Zirconia ceramic materials. All structures have been printed using one of the additive manufacturing processes known as Fused Filament Fabrication (FFF) (Smirnov et al., 2023; Terekhina et al., 2022). The idea consist to study the link between the relative density and the specific energy absorption (SEA) capabilities of the structure, and consider how to increase the SEA by controlling the damage to the structure like sponge do it.

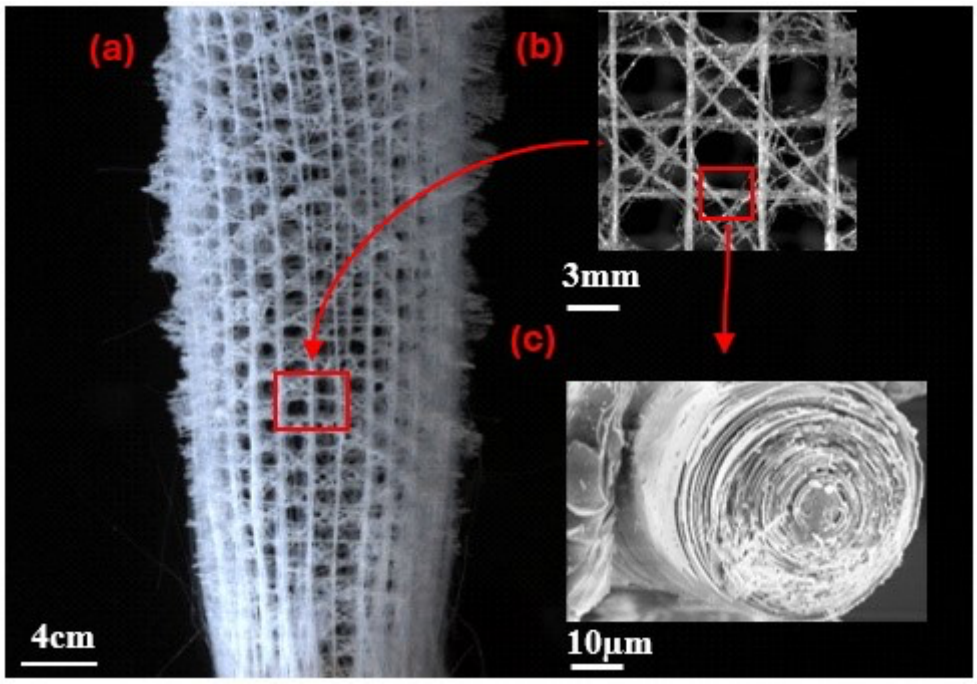

Figure 2: Euplectella aspergillum skeletal structure. (a) Photographic image of a cleaned sponge specimen showing the full skeletal structure, (b) At higher magnification, the square-grid architecture and regular ordering of the vertical and horizontal components of the skeletal system are clearly visible, (c) Laminated organic/inorganic hybrid structure of the spicules. Copyright reserved for this image (Hassan's PhD project 2022-2025).

Personally, the motivation for this study, relies on the gap in the research database, the possibility of finding solutions to modern problems and the possibility for applications related to civil engineering which is my previous field of studies.

2. Bibliography

2.1 Fused Filament Fabrication (FFF)

Among the different available additive manufacturing techniques, fused filament fabrication (FFF), is widely spread and this is the only process that is used for four kinds of materials: polymers, composites, metals and ceramics (Auffray et al., 2021; Terekhina et al., 2022; Smirnov et al., 2023; Ramazani et al. , 2022). The FFF process consists of heating a thermoplastic filament slightly above its melting point inside a nozzle, extruding the viscous material out of a die and deposit it sequentially and additively, according to the programmed path corresponding to the G-code file. FFF offers advantages when compared to other techniques in areas such as ease of use, post-processing needs, environmental considerations, and the investment cost for an individual device. Compared to other additive manufacturing processes, the equipment used can be inexpensive and very easy to operate. Below, I will focus in details of the FFF process of ceramic.

2.1.1 Fused Filament Fabrication of ceramics

The fused filament fabrication of ceramics (FFFC) is the trendiest technique and represents a relatively novel approach to ceramic production. The idea of using highly filled polymers for the additive manufacturing of metal and ceramic parts was first introduced in the 1990s; it was named fused deposition of metals (FDMet) and fused deposition of ceramics (FDC), respectively. It was based on the Stratasys FDM technology in which highly filled polymers with metal or ceramic particles are initially extruded as filaments, and then these filaments are selectively extruded at a temperature higher

than the melting point of the binder polymer. By filling thermoplastics, considered the binder, with ceramic powder in very high solid contents (>45%), it is possible to print objects that can be debinded and sintered to attain densities comparable to those fabricated via conventional approaches (Cano et al., 2019; Orlovská et al., 2020; Smirnov et al., 2023). The debinding step consists of removing the binder from the parts. As the binder system used for FFF includes more than one type of polymer, two-step debinding is required. For this purpose, chemical debinding followed by thermal debinding is usually performed. During chemical debinding, the part is immersed in a chemical that dissolves the support polymer, resulting in the formation of pores in the part. These pores enable the removal of the high-melting-point backbone polymer from the part during thermal debinding. For thermal debinding, the part is exposed to high temperatures. Following debinding, in order to fuse particles and reach high densities, sintering is applied at high temperatures. Sintering is the consolidation of the part and is a straightforward step in ceramic processing if the homogeneous particle packing in an as dense as possible ceramic green body is provided during shaping. The driving force for sintering is the reduction of the surface energy resulting from the neck formation between particles. Growth of neck between particles is referred to as coarsening. Coarsening is followed by densification where the centers of particles get closer to each other (Gonzalez-Gutierrez et al., 2018; Smirnov et al., 2023). The schematic representation of the shaping, debinding and sintering process for fabrication of the metal and/or ceramic components is presented in Figure 3.

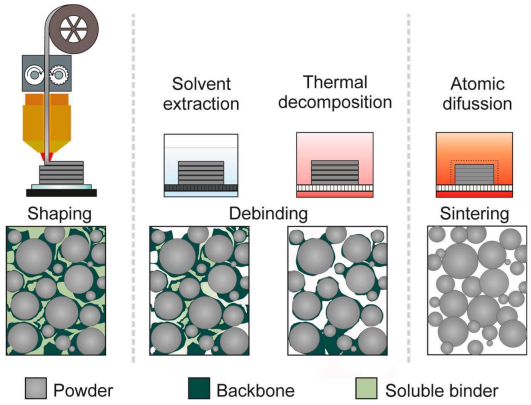

Figure 3: Schematic representation of the shaping, debinding and sintering process and respective morphology of the parts for the fabrication of metal, ceramic, or metal-ceramic components (Gonzalez-Gutierrez et al., 2018)

Recently, commercial filaments emerged for FFF ceramic, including alumina and silicon carbide based systems from Nanoe (Nanoe, 2020) and zirconium silicate filament from Virtual Foundry (Virtual Foundry, 2023). All commercially filaments that are readily available in the market share certain features; their suggested nozzle diameter is consistently a minimum of 0.6 mm, and they tend to be brittle. In the case of Virtual Foundry, they advise pre-heating the feedstock before it reaches the feeder to avoid breakage. On the other hand, Nanoe's ceramic composite filaments can only be used with a designated printer that is equipped with a direct-drive filament system (such as Raise 3D, Prusa, FlashForge…) (Smirnov et al., 2023).

2.2 Manufacturability of lattice structures

A lattice structure is an architecture formed by an array of spatial periodic unit cells with struts, edges, and faces. The manufacturability of a lattice structure refers to the ease of fabricating the structure by a certain AM process. In order to choose the right AM process, factors like the candidate material, the process resolution, the ease of support removal and the manufacturing cost should be taken into consideration. The minimal strut size determines the smallest feature and constrains the minimal unit cell size that can be achieved in the lattice structure, which is influenced by many factors. For example, in SLM process, powder particle size, laser spot diameter, laser power, and laser scanning speed, all have direct influences on the minimal strut size. When a finer powder and a smaller laser spot are

employed, thinner struts will result. Another factor constraining the minimal size of a unit cell is the level of difficulty of removing the unused powder after part fabrication. Whereas, in FFF process, nozzle diameter, nozzle temperature and printing speed directly impact the minimum strut size. All AM processes follow the layer-by-layer concept, necessitating the bonding of the next layer onto the current one. When there is no contact interface between the two layers, or the contact interface is too small, sacrificial structures are needed to support the next layer or to minimize potential deformation. However, support structure is not expected in lattice structure fabrication, for it is difficult or even impossible to be removed inside the lattice structure. Therefore, a lattice structure is required to have its own self-support property. Exceptions are: (i) FDM process which can use a soluble material to build support structures that are easy to be removed afterwards and (ii) SLS process whose unused powder in the bed can provide support function. The classification of the different cellular structures is presented in the Figure 4.

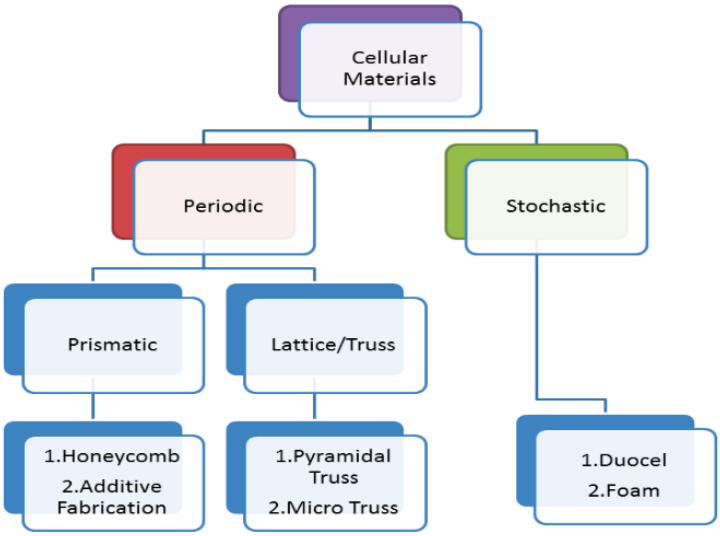

Figure 4: Classification of cellular structures (Asbhy et al. 2000)

In addition to the periodic and stochastic categories, there exists a third category not shown in Figure 4. This category includes structures that combine the isotropic characteristics of stochastic structures, such as foams, with the ease of studying the unit cell found in periodic structures. These structures are known as quasi-periodic lattices (Somera et al., 2022).

2.3 Design methods for lattice structures

From the perspective of structural design, a lattice structure can be generated by a unit cell's repetition following a certain spatial patter. Thus, the design of a lattice structure includes unit cell design and pattern design (Tao and Leu, 2016).

2.3.1 Unit cell design

A general lattice material is defined as a cellular, reticulated, truss or lattice structure made up of a large number of uniform lattice elements (e.g. slender beams or rods) and generated by tessellating a unit cell, comprised of just a few lattice elements, throughout space. The unit cell is defined as the smallest element making up and characterizing the whole lattice structure. One can employ various design approaches, such as a primitive-based method where the unit cell comprises geometric primitives, an implicit surface method defining the unit cell surface through mathematical equations, or a topology optimization method, which derives cell geometry through optimization calculations. Before additive manufacturing, the fabrication of complex geometries like lattice structures especially with a very small unit cell was extremely difficult.

2.3.2 Pattern design

As mentioned before, a lattice structure can be generated by a unit cell's repetition following a certain spatial pattern; thus, the design of a lattice structure includes not only the unit cell design but also a pattern design. Pattern design involves the repetition of unit cells in 3D space, and it can be achieved through three distinct methods. The first is direct patterning, where unit cells are repeated translationally. The second is conformal patterning, wherein units are repeated to conform to a specified surface geometry. Lastly, topology optimization is employed, not only to optimize material distribution within a single unit cell but also to organize the spatial replication of the unit cell throughout the entire design space.

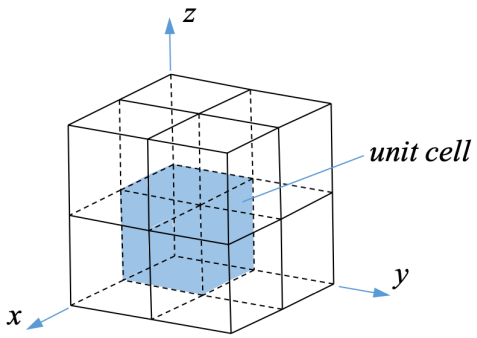

Figure 5: Schematic of direct patterning (Tao and Leu, 2016)

2.4 Mechanical behaviour of lattice structure design consideration

The mechanical behavior of a lattice structure depends on the material, the architecture, and the porosity of the structure but the constituent material determines the mechanical properties such as Young's modulus, yield strength, brittleness, ductility, etc. The implementation of a lattice structure instead of a solid one, provides more mechanical flexibilities enabled by the appropriate lattice architecture design.

2.4.1 Maxwell stability criterion

Triangulated truss structures (known as space-frames in 3D space) provide a fundamentally efficient structural system. Such truss structures are typically designed to ground internal and external loads by a combination of tensile and compressive axial loading within the associated strut elements. For external loads to be robustly equilibrated by internal forces within the truss structure, a sufficient number of strut elements with appropriate nodal connectivity must exist. Maxwell proposed a set of mathematical conditions that must be satisfied for the loads to be grounded in a mechanically robust manner. The Maxwell stability criterion states that there are 2 free equilibrium equations (3 for 3D space) associated with each node j, and that each strut, s, represents an unknown equilibrium force; furthermore, there are 3 external forces (3 for 3D space), resulting in the inequalities of equation (1) and (2).

$M = s - 2j + 3 = 0$, for planar (2D) truss systems (1)
$M = s - 3j + 6 = 0$, for 3D space-frames (2)

For $M < 0$, there are insufficient struts to equilibrate the external forces, and the jointed space frame is unstable and becomes a mechanism, the struts tend to bend under external loading, leading to a bending-dominated architecture (Figure 6(a)). For $M = 0$, the strut elements are arranged such that the strut loading is determinant for any external loading; such structures are defined as just-stiff and contain no structurally redundant struts elements (Figure 6(b)). Additional strut elements can further increase the Maxwell number, $M > 0$, making the truss over-stiff. For the last two cases, the struts can carry compressive or tensile loading, leading to a stretching-dominated architecture (Figure 6(c)).

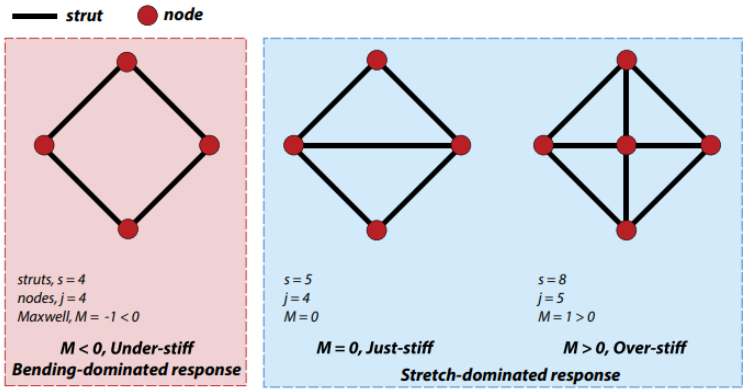

Figure 6: The pin-jointed frame at (a) folds up when loaded-it is a mechanism. If its joints are welded together, the struts bend- it becomes a bending dominated structure. The triangulated frame at (b) is stiff when loaded because the transverse strut carries tension-it is a stretch-dominated structure. The frame at (c) is over constrained ; if the horizontal bar is shortened the vertical one is put into tension even when no external loads are applied (giving a state of self stress) (Ashby, 2006).

2.4.2 Observed mechanical response (unit cell)

The Maxwell stability criterion (J. Clerk Maxwell F.R.S.,1864) enables a profound insight into the mechanical response of lattice topologies. For AM lattice structures that are under-stiff ($M < 0$), lattice deformation is resisted by bending at the nodes. Due to the large strains induced by the associated bending stresses, these structures are highly compliant, and are known as bending-dominated. Conversely, for structures that are either just stiff ($M = 0$) or over-stiff ($M > 0$), loads are grounded by tension and compression of the strut elements only, and there is no bending applied across the node. These structures are known as stretch dominated ($M \geq 0$) and display relatively high stiffness.

It is observed that, the modulus and initial yield strength of a stretching-dominated cellular solid are much greater than those of a bending-dominated cellular material of the same relative density. This makes stretching-dominated cellular solids more suitable compared to a bending-dominated one for lightweight structural applications. It is noteworthy that, in compression, the stretching-dominated materials have a softening post-yield response due to the buckling of the struts (Deshpande et al., 2001). Thus, these materials may be less attractive as energy-absorbers since this application requires a stress-strain response with a long, flat plateau.

2.4.3 Prediction of AM lattice response

Numerous predictive models have been established to relate the lattice topology and material properties to the observed mechanical properties, most notably the Gibson-Ashby model (Gibson and Ashby, 1982). The model is semi-empirical because its scaling exponents were derived analytically but its scaling prefactors were empirical. Specifically, the model predicts that the lattice mechanical response, P, is proportional to some known response of the solid material P_s, and the ratio of lattice to solid material density, ρ/ρ_s, to the power of some exponent, n, and scaled by some proportionality constant C, depending of geometry cell. The predicted exponent depends on whether the structure is bending- or stretch-dominated as summarized for a number of pertinent scenarios as follows (Zhong et al., 2023):

$$E^* = C\, E_s \left(\frac{\rho}{\rho_s}\right)^n \qquad (3)$$

$$\sigma^* = C\, \sigma_s \left(\frac{\rho}{\rho_s}\right)^m \qquad (4)$$

Where σ^*, and E^* denote the yield strength and the elastic modulus of solid parent material, respectively. The values of power indices n and m depend on the deformation mode. Based on the theoretical model, the index n should be equal to 2 and 1.5 for bending-dominated and stretching-dominated structures, respectively. While the index m should be equal to 2 and 1 for bending-dominated and stretching-

dominated structures respectively. However, previously published results have shown that n and m values might lie between, below or above the theoretical values regardless of structures deformation behavior based on the Maxwell criterion (Maconachie et al., 2019). Despite its limitations, this set of equations constitutes a useful tool for lightweight applications, where structures are designed to have high strength with the lowest possible density. However, when designing a scaffold for orthopedic surgery, maximizing strength in terms of stiffness (elastic modulus) is more critical. By combining these two equations, a modified expression of Gibson-Ashby model can be obtained:

$$\frac{\sigma^*}{\sigma_s} = C_3\left(\frac{E^*}{E_s}\right)^{\frac{n}{m}} \qquad (5)$$

The Maxwell stability criterion can be used to directly characterize the lattice response as being either bending- or stretch-dominated. From this understanding, the Gibson-Ashby model can be utilized to predict the specific mechanical response of the associated lattice system. These predictions are compatible with the experimentally observed mechanical response of AM lattice structures.

2.4.4 Mechanical response of lattice structure in compression

The typical stress-strain curves of lattice structure in compression mode is characterized by three distinct regimes, as illustrated in figure 7a: (i) an initial linear elastic region until the struts yield due to bending or stretching, (ii) a roughly constant stress plateau region, corresponding to cell collapse by buckling (Fig.7b), yielding (Fig.7c), or fracture (Fig. 7d) depending on the kind of material and the morphology (extending up to large strains, typically 70–80%); (iii) and a final sharp increase in stress with further strain, corresponding to densification of the material, with opposing cell edges and faces compressed against each other (, Ashby et al., 2006, Gibson et al.,1999, Benedetti et al., 2021).
The main objective of doing compression test is to evaluate energy absorption of the structure. In this test, specific energy absorption (SEA), efficiency (η), module Young's (E) and the onset of densification (ε_d) are most important parameters that should be considered (Li et al.,2006).

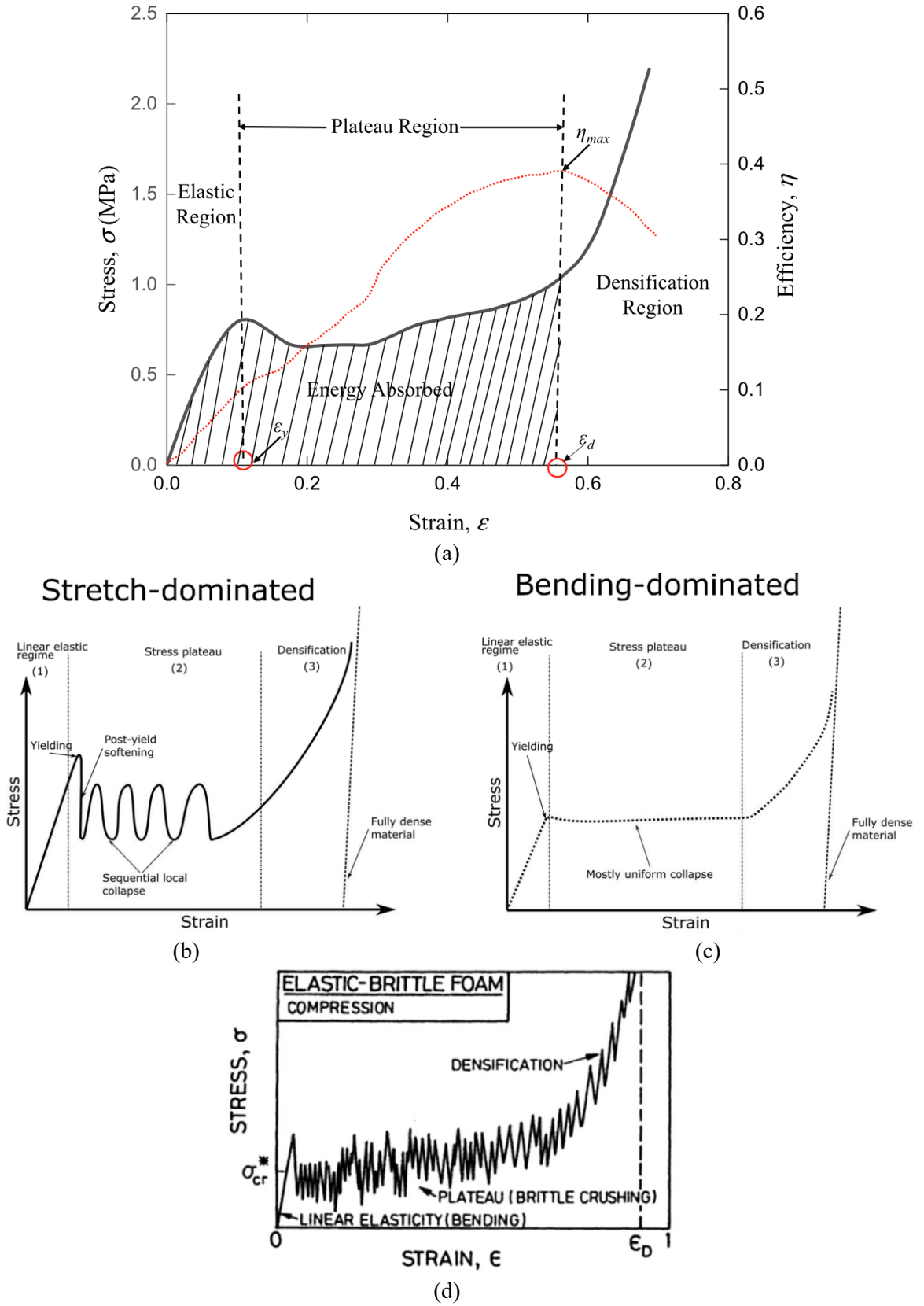

Figure 7. (a) Stress vs. strain (solid black curve) and efficiency vs. strain (dotted red curve) plot showing different energy absorption parameters and regions; Compressive strain-stress curves for (b) stretching-dominated, (c) bending- [Benedetti, 2021] and d) fracture-dominated cellular materials [Gibson and Ashby, 1999]: (1) Linear-elastic regime, (2) Post-yield stress plateau, (3) Densification.

2.5 Biomimetics and structural engineering

2.5.1 Biomimetics application

Biomimetics and be inspired by nature is not a new concept since its application regarding energy absorption was first tested in 2000. With the demand for lightweight structures with high energy absorption capacity increasing for numerous applications such as aerospace and civil engineering, scientists and engineers tried to study and obtain these properties from biological structures which, through years of evolution, are capable to adapt to various extreme environments.

By studying plants and animals found in nature, one can observe the desired characteristics such as low density, high strength, and high energy absorption capacities. Some examples of these structures include the pomelo fruit with a unique spongy mesocarp layer that can dissipate energy of 80 J from free fall tests without leading to visible outer damage of the peel (Fischer et al., 2010). Similar information regarding energy absorption can also be found in animals, like the beetle whose forewing can withstand a puncture force up to 23N, which is much higher than the fighting force of the beetle (Ha et al., 2018; Ha and Lu, 2020) (Figure 8). Overall, biological materials and structures exhibit extraordinary energy absorption capacity and provide inspiration for the design of new energy absorbers, making bio-inspired structures a promising solution for the future.

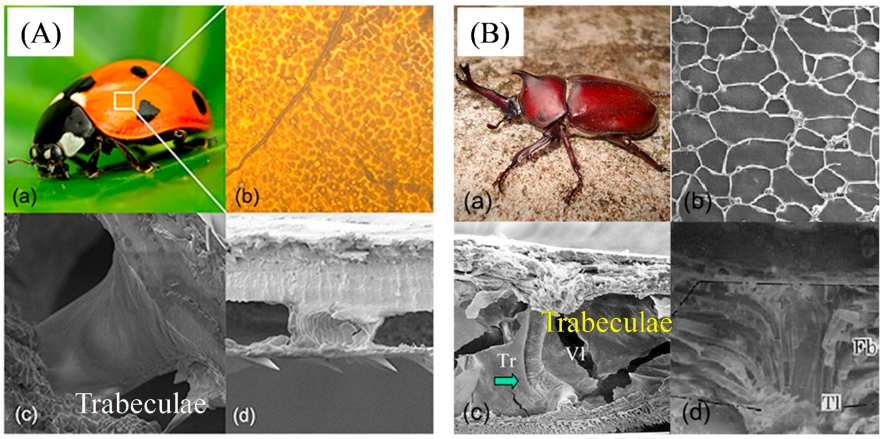

Figure 8: (A) Ladybeetle forewind microstructures, (B) Japanese beetle forewing microstructures (Ha and Lu, 2020)

Regarding the application of these structures in the macro scale, the biomimetic approach has been applied in civil engineering for the development of bio-inspired materials and structures with high impact resistance and toughness (Sun et al., 2015) (Figure 9). Sun et al. conducted a study on the drop-weight test impact response of a building ceramic composite with a nacre-like structure. The results demonstrated enhanced impact resistance in the composite when compared to a basic layered ceramic composite that consisted of nonpartitioned tile layers.

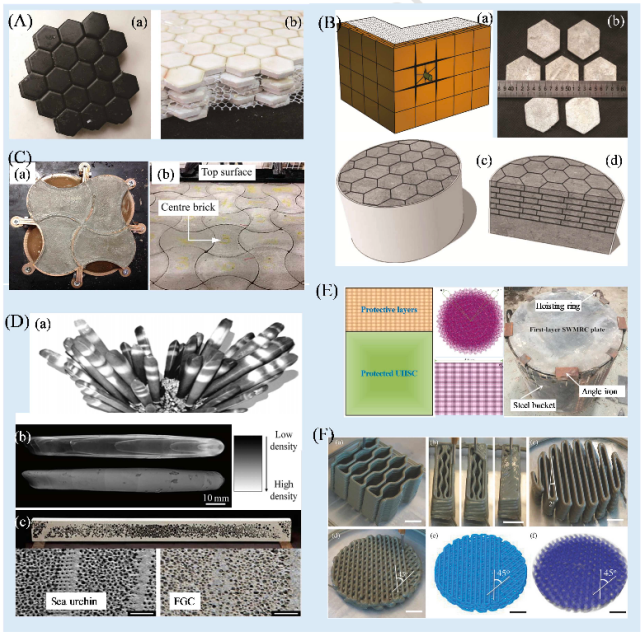

Figure 9: Bio-inspired structures for civil engineering; (A) building ceramic composite with a nacre-like structure; (B) bricked- wall structure ; (C) interlocking concrete mimicking nacres structure ; (D) FGC mimicking the structure of sea urchin spines ; (E) concrete structure with staggered arrangement of steel wire mesh ; (F) Bio-inspired 3D printed concrete (Ha and Lu, 2020)

In the examination of various structures, the focal point of this study lies in the investigation of bio-inspired cellular structures and more specifically bio-inspired lattices. The classification of bio-inspired structures is summarized in Figure 10. While biomimetics in past years primarily concentrated on surface properties, such as achieving a non-slip surface, contemporary advancements in additive manufacturing have expanded its scope to encompass properties related to the volume of structures, facilitating the creation of lightweight and efficient structures.

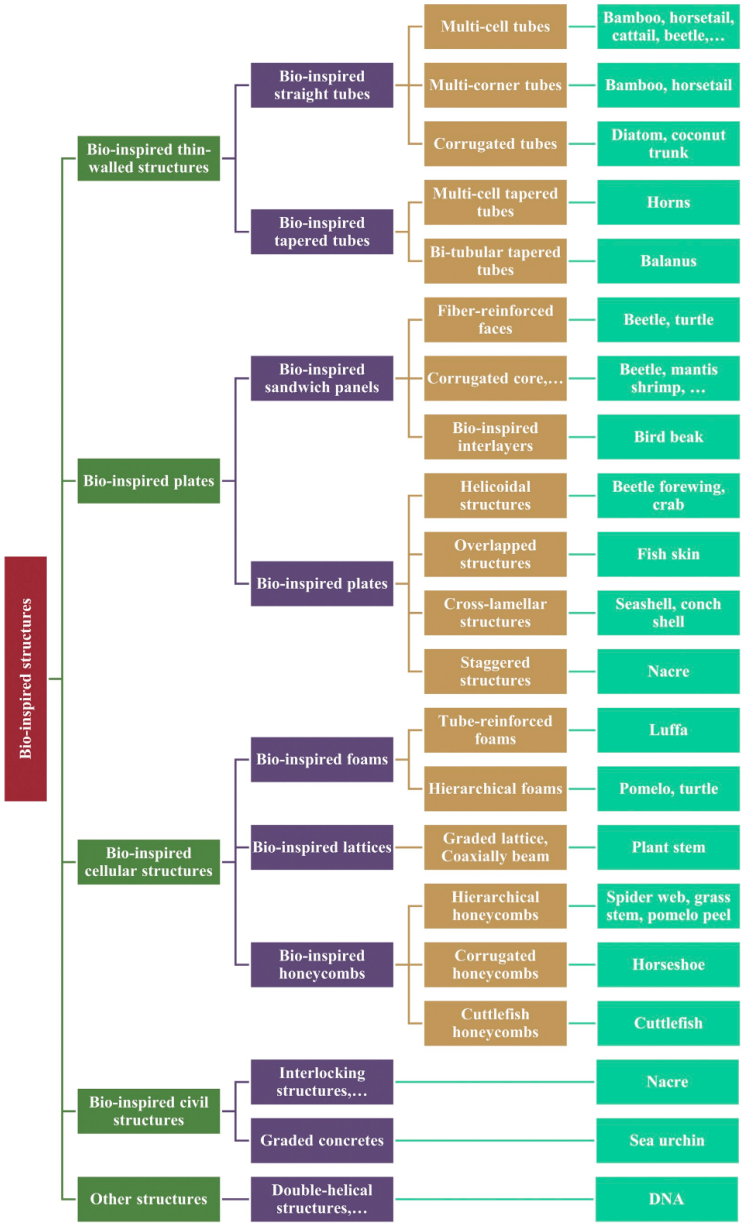

Figure 10: Categories of bio-inspired structures (Ha and Lu, 2020)

2.5.2 Skeleton of Euplectella sponge

Focusing on the structure of the Euplectella sponge, the surface of the cylindrical skeleton consists of a regular square lattice with series of vertical and horizontal silica struts. Each silica strut is composed of bundles of spicules which during its lifespan progresses from an easily deformable phase, consisting of loosely bonded spicules, through various stages of skeletal consolidation, eventually resulting in the rigid form. The cell spacing between vertical and horizontal struts is about 2.5 mm, while the diameter of each strut is about 0.25 mm. These struts are incorporated with a set of diagonal elements, interconnecting in a way that generates a series of alternating closed and open cells (Figure 2). The function of diagonal struts is to prevent buckling of sponge under the high pressure present deep inside the seam and helps to absorb vibrations caused by the vortexes which forms during the flow of sea water from one end to the other end of the sponge. The combination of horizontal, vertical, and diagonal struts results in a neat optimal strut-based design.

Scientists and engineers have been drawn to this structure due to its remarkable hierarchical architecture and mechanical robustness across multiple length scales. Grid-like open-cell structures, like those observed in the skeletal system of the Euplectella sponge, are frequently utilized in engineering

applications due to their lightweight nature, excellent energy absorption capabilities, and effectiveness in managing the transmission of acoustic and thermal waves.
In the investigation of mechanical properties, (Fernandes et al., 2021) utilized a combination of experimental and numerical analyses. By implementing an optimization algorithm to identify the optimal beam configuration in a diagonally reinforced square lattice for achieving the highest critical load, the study revealed the Euplectella sponge's skeletal system to be remarkably close to this design optimum. These findings confirm the effectiveness of biomimetics in modern applications and offer valuable insights for tailoring lattice architectures to attain enhanced and robust outcomes in design. Regarding the microstructure, the spicules of the sponge consist of a concentric lamellar structure, where the thickness of the layers decreases from approximately 1.5 µm at the center to about 0.2 µm at the periphery of the spicule and are separated by organic interlayers (Aizenberg et al., 2005). The presence of these interlayers can introduce internal stresses within the structure, similar to pre-stressed reinforcement in concrete, which can impede crack propagation along the interface (Dunlop et al., 2011) (Pokroy et al., 2009).

3. Scientific approach

In this research, a multi-scale scientific methodology was employed. The initial focus was on the sponge's microstructural element (Figure 11b), the spicule, which was subjected to physicochemical (EDX analysis- see Figure 16, and 17) and mechanical evaluations (3 point bending test) (Figure 13). These assessments aimed to define the sponge's attributes, encompassing both its material composition and elastic mechanical traits. Following this, with a clear understanding of the spicule's properties, the research progressed to examine the energy absorption potential of a ceramic structure inspired by the sponge's mesostructure (See Fig 11b, and 32).

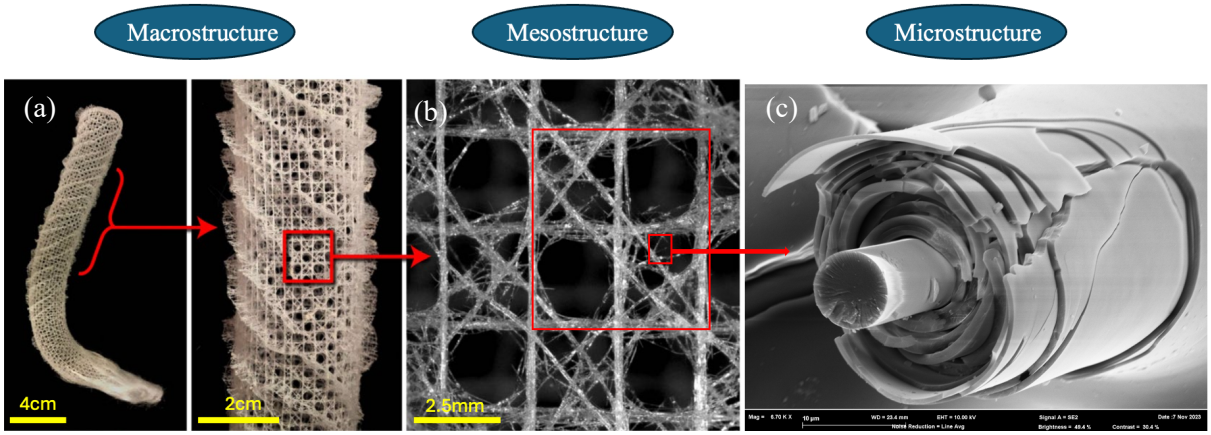

Figure 11: (a) Euplectella aspergillum skeletal structure (Fernandes et al., 2021), (b) The square-grid architecture and regular ordering of the vertical and horizontal components of the skeletal system, (c) Laminated organic/inorganic hybrid structure of the spicules (Hattali, Terekhina, Caillault, Fotiadis) .

3.1 Physicochemical and mechanical analysis of microstructure

3.1.1 Main idea

In this part, two characterization processes will be performed, a physicochemical analysis and a mechanical 3-point bending test. The first test is to verify the glassy composition of the sponge and the second one to calculate the Young's modulus and compare the results with the existing literature.

3.1.2 Tools

The first step was the study of the spicule by Scanning Electron Microscopy (SEM) (ZIESS SUPRA 25). This will allow us to verify the concentric cylinder structure that is mentioned in literature and to study the sponge's structure in depth. In addition to the microscopy observation, an EDX analysis was performed to study and verify the composition of the spicule. To determine the Young's modulus of the spicules, we used a 3-point bending test, performed using the Anton Paar Bioindenter: UNHT³ Bio (Fig.12-13). The instrument is widely used to study the local mechanical properties of materials of various origins, including biological ones. The idea here is to use the indenter with a spherical radius (approximately 250 µm) as a rod that applies a constant displacement (v=5 µm/min) to the spicule (diameter ~ 50-60 µm) until reaching 15,00 µm of deflection. The instrument is equipped with a force sensor capable of measuring forces on the order of 1µN, thus providing us the load versus displacement curve of each test. No less than a dozen tests have been carried out with some of them invalid due to issues such as slippage of the spicule and incorrect positioning of force application.

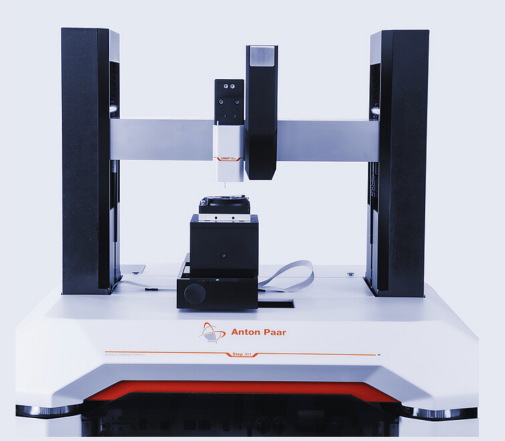

Figure 12: Anton Paar Bioindenter: UNHT³ Bio

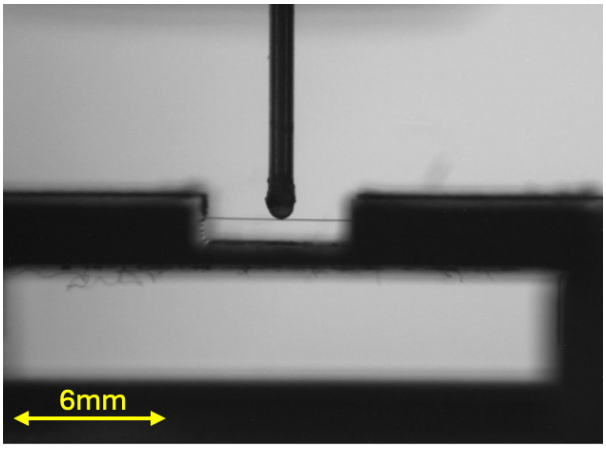

Figure 13: 3-point bending test configuration

To perform the test, a custom support for the spicule was designed and fabricated using Prusa MK3 (Fig.14).

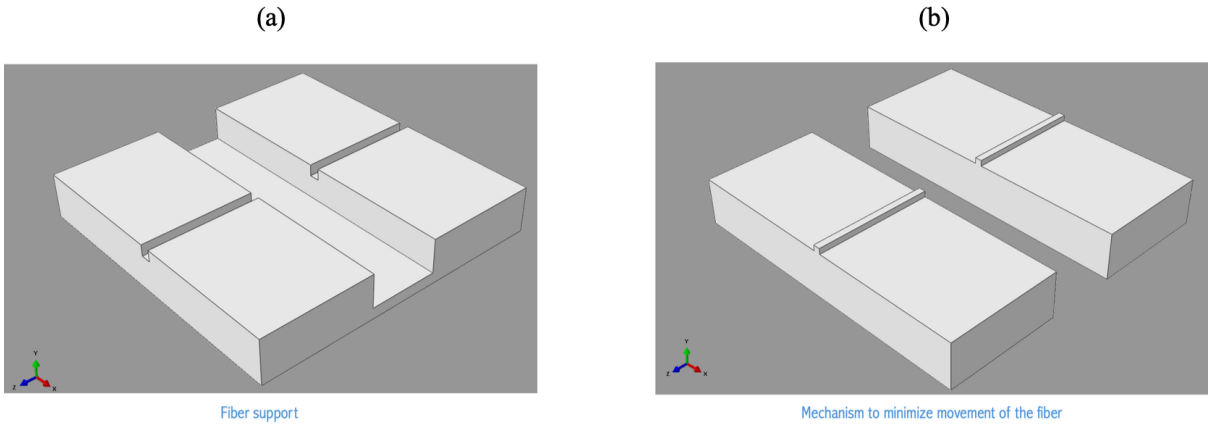

Figure 14: Support configuration for 3 point bending test, (a) lower support, (b) upper support.

By using this configuration, the fiber is placed on the left part (lower support), glue is applied and then the right part (upper support) clicks on top to assure there will be no movement during the test. By assuring that, the formulas for a double-encastrated beam can be used. The obtained result from the test is a force-displacement graph. After determining the slope (S) of the graph, the following formulas are used to calculate the Young's modulus.

$$E = \frac{S * l^3}{192 * I} \tag{6}$$

$$I = \frac{\pi * d^4}{64} \tag{7}$$

Where:
S: slope of the linear data obtained from force-displacement curve,
l : the length of the spicule between two supports (~ 6mm),
I : is moment of inertia,
d: diameter of the spicule (diameter ~ 50-60 µm)

3.1.3 Results

The sectioned spicules from EA contained between 12 and 35 silica cylinders each. In most analyzed images, the complete boundaries of all of the cylinders were not easily identifiable due to the complex fracture patterns induced by sample sawing. The images highlight the brittle behavior of spicules (Figure 15). Without being able to quantify it, it seems that the thickness of each cylinder decreases from the inside to the outside.

Weaver et al show that each spicule is made up of micron thick concentric rings of nanoparticulate silica separated by 5 – 10 nm thick layers of proteinaceous "glue". This soft glue although not yet fully characterized, consists of chitin and collagen like proteins, the properties of which are strongly modified by the presence of water. In our case, it was not possible to analyze the existence of such a protein because the sponge obtained for the study had already been washed with a slightly acidic product and dried. However, EDX analysis has revealed the existence of chemical components such as Si, O, Na and Cl, by confirming the spicule made of a silica-type glass (SiO_2) and residues of NaCl sea salt (Figure 16 and 17).

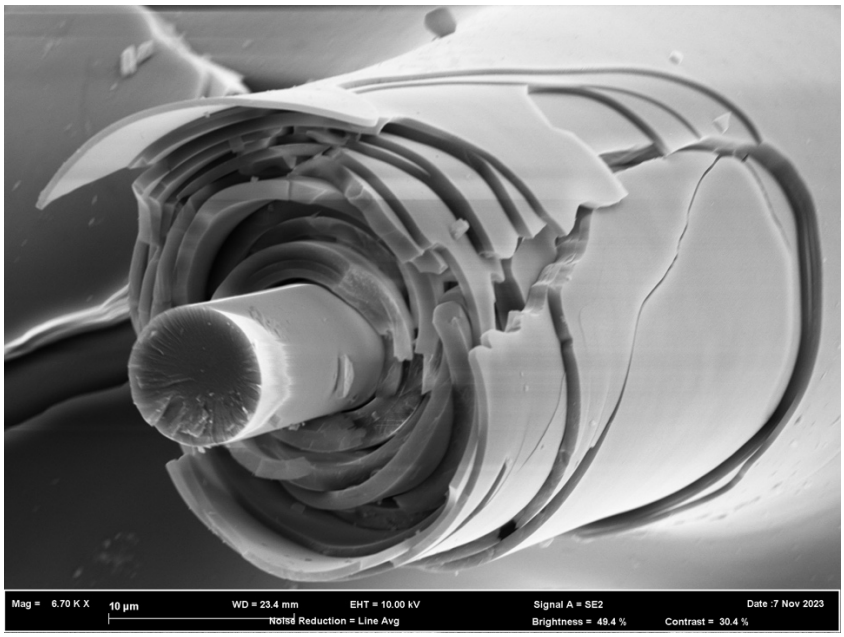

Figure 15: The structure of the spicule, obtained with scanning electron microscopy. Copyright reserved for this image *(Hattali, Terekhina, Caillault, Fotiadis).*

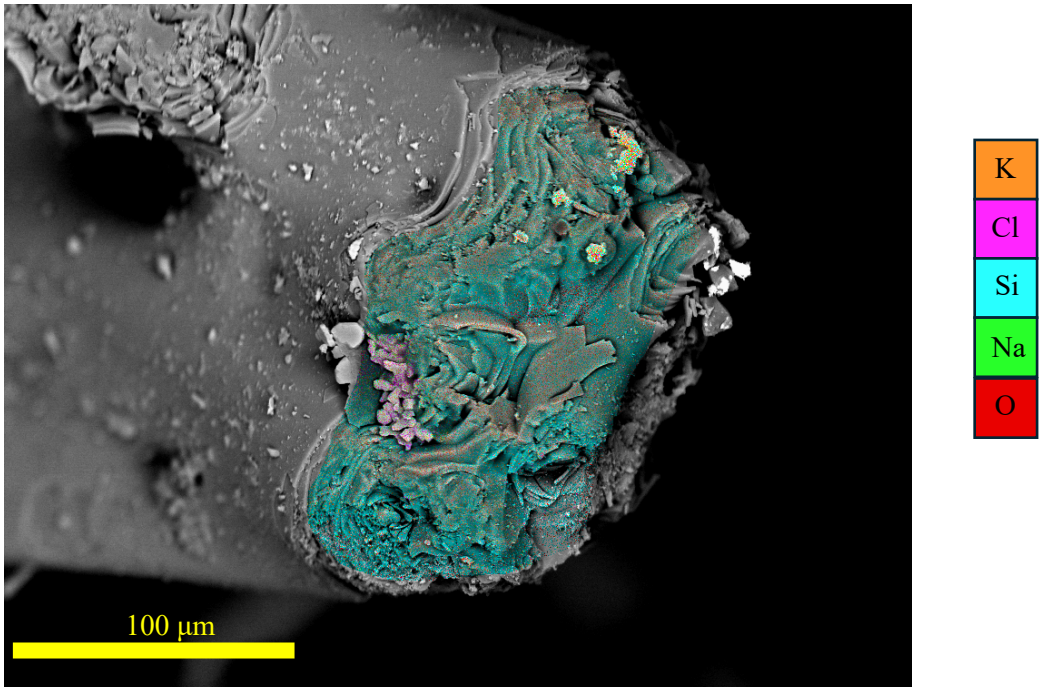

Figure16: EDX analysis on spicule

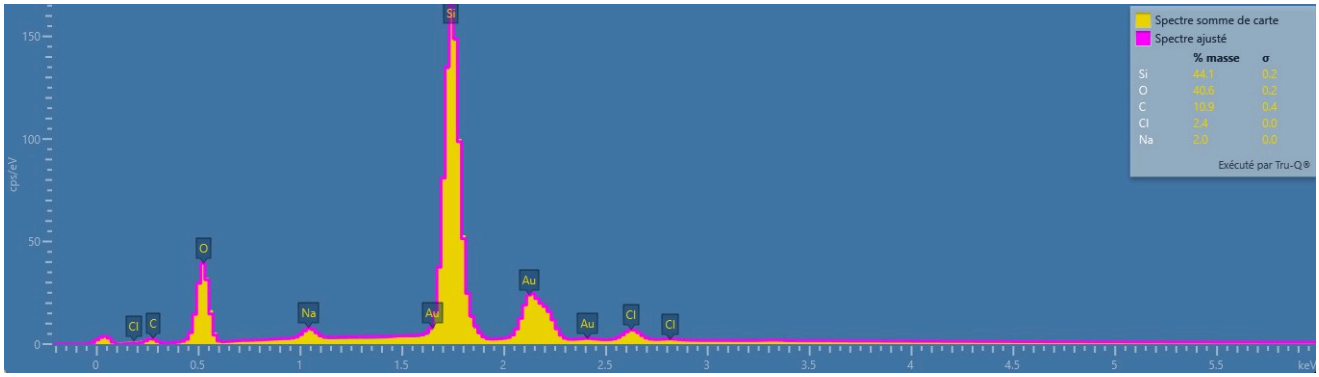

Figure 17: Spicule's composition

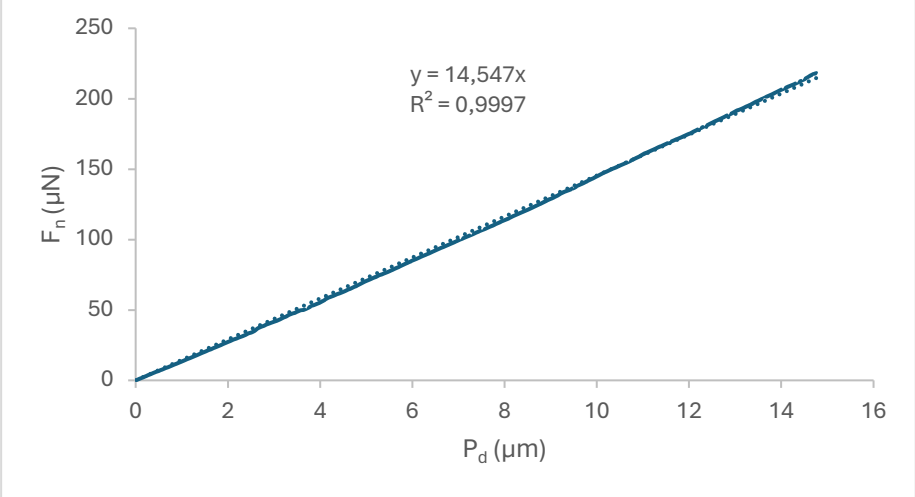

Figure18: Typical Force displacement curve from 3-points bending test

From the slope of graph and by using the aforementioned formulas, the Young's modulus can be calculated and summarized in Table 1.

Table 1: Young's modulus determination

Slope (N/mm)	L (mm)	Diameter (mm)	I (mm4)	E (Mpa)	E (Gpa)
0.014988	6	0.05394	4.15541E-07	40577.25	**40,58**

The results obtained by our method (~ 40 GPa) are equivalent to the results obtained by Miserez et al through nano-indentation (~ 42 GPa) who show that the silica modulus from the spicule core varies slightly with the applied load and is only about half of the respective values for the fused quartz (68 GPa), a difference attributed to the hydrated nature of the silica in the spicules.

Nevertheless, we have some reservations concerning our tests. Upon comparing the results from various tests, an inconsistency was observed. Further analysis indicated that this was due to errors in measuring the diameter. Given that the average diameter of the sponge's spicule is 50 um and measurements were taken using an optical microscope, achieving exact diameter measurements was challenging. The impact of this measurement error on the Young's modulus is illustrated in Figure 19. An error in the measurement of the spicule's diameter of 5% (in our case 0.1 µm) results in an error in the estimation of Young's modulus of 22.8 %. The use of a scanning electron microscope is essential to achieve precision in our estimates.

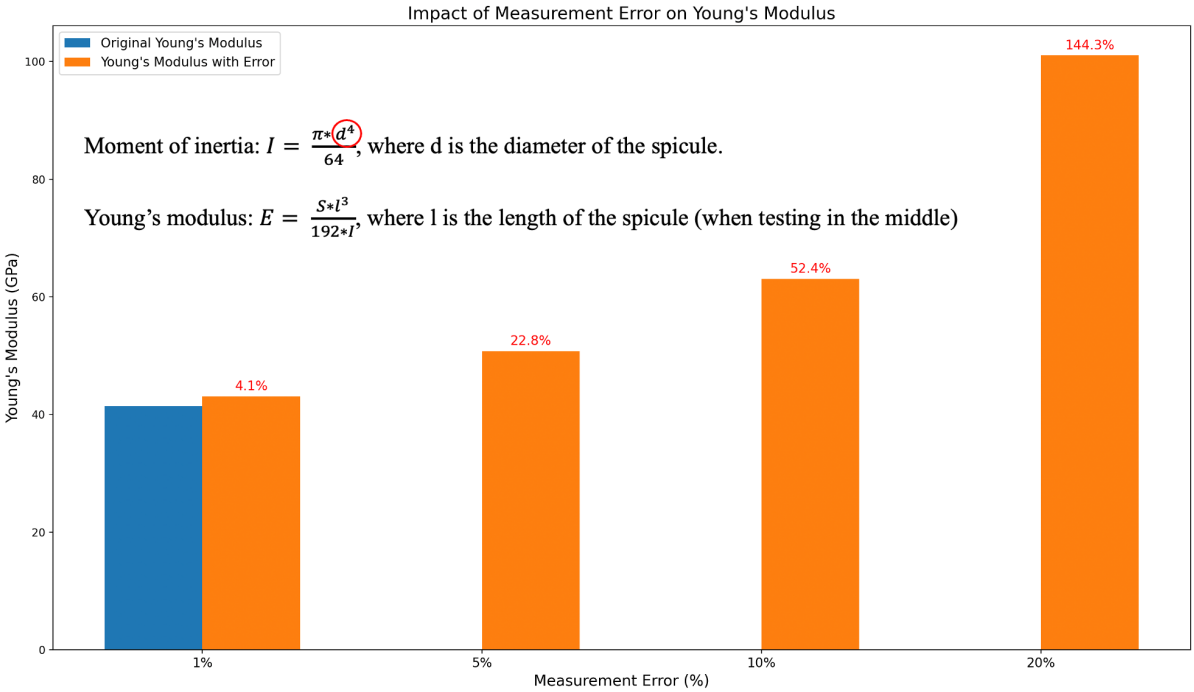

Figure 19: Impact of measurement error on Young's modulus

3.1.4 Summary

Through the study of the microstructure, the information available in literature was verified and a deeper understanding of the spicule structure was achieved. More specifically, a Young's modulus of 40 GPa was found, using a relatively simple method. This result is aligned with the work of *Woesz et al.2006, and* Miserez et al 2007, where a much more complicated method was used to mechanically characterize the sponge's spicule. The SEM images show the complex structure of each spicule. Unfortunately, we have not succeeded in quantifying the number of concentric cylinders as well as the thickness of each ones. This work requires meticulous preparation of the spicules. Future studies planned could delve deeper into this aspect and will provide even more detailed information on the resilience of the sponge.

3.2 Mesostructure

3.2.1 Main idea

The developed main ideas in this section consist of reproducing the aforementioned bio-inspired structure using lightweight ceramic materials and study the link between their relative density and the specific energy absorption (SEA) capabilities. Given the inherent fragility and limited toughness of ceramics, our approach draws inspiration from sponge spicules that create a multilayered material using silica glass (as the rigid component) separated by a protein-based material (the soft component) and consider how to increase the SEA by controlling the damage to the structure like the sponge does. To achieve this, we coated ceramic samples with a thin layer of epoxy and compared energy absorption during compression tests with uncoated ceramic structures. The main pillars of the scientific approach are presented in Figure 20.

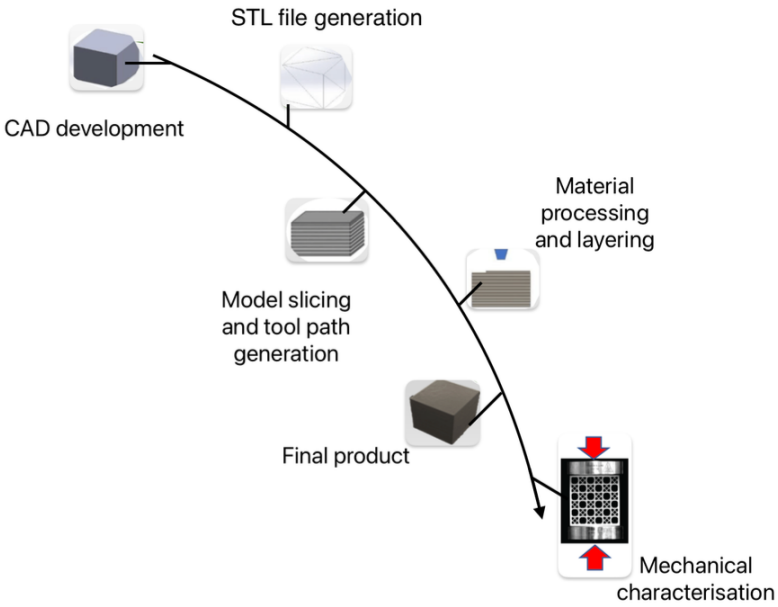

Figure 20: Scientific approach

To demonstrate our design strategy and explore the effect of altering relative density on mechanical energy absorption, a quasi-static uniaxial compressive test, along the y-direction, was carried out by using the Instron 5882, an electro-mechanical multi-space machine with a maximum load of 100kN at room temperature.

3.2.2 Materials

The choice of materials lies in various factors. The commercially available materials, materials with applications in engineering fields and materials that have some similarities in terms of fragility compared to silica spicules. By considering all these factors, the materials that were chosen are the ceramics: (i) Alumina (Al_2O_3) and (ii) Zirconia (ZrO_2). For that, Zetamix filaments (Zirconia (ZrO2) and Alumina (Al_2O_3)), produced by Nanoe (France), were used to print bio-inspired samples. One big challenge with Zetamix Alumina filaments is that they are very brittle. To avoid this issue, we have completely revised the filament extrusion system of our Prusa MK4 printer. A Table 2 with the characteristics of each material is presented below.

Table 2: Mechanical properties of the used materials

Material	Young's Modulus (Gpa)	Fracture Toughness (Mpa√m)
SiO_2	66.3-74.8	0.62-0.67
Al_2O_3	215-413	3.3-5
ZrO_2	100-250	1-3

The materials are in the form of ceramic filaments. Their composition constitutes of a binder polymer and the ceramic particles. The composition for the two filaments used in this study is presented in Table 3.

Table 3: Filament composition(Zetamix by Nanoe)

Material	Weight percentage (%)		Volume percentage (%)	
Al_2O_3	**Binder polymer**	**Ceramic particles**	**Binder polymer**	**Ceramic particles**
	17	83	55	45
ZrO_2	**Binder polymer**	**Ceramic particles**	**Binder polymer**	**Ceramic particles**
	14	86	50	50

3.2.3 Tools

To create the samples, the FFF additive manufacturing technique was used and the corresponding cycle is shown below (Figure 21).

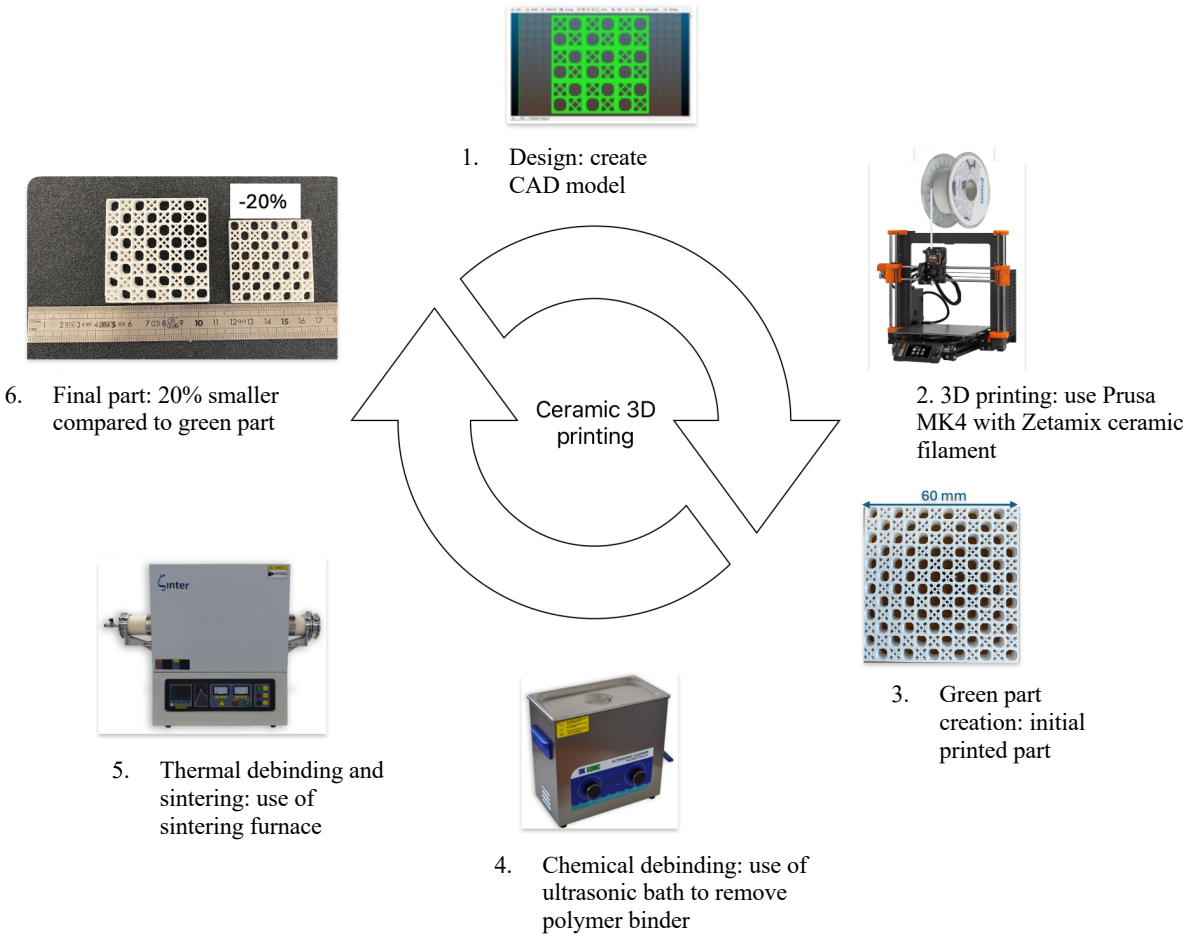

Figure 21: FFF process for ceramic materials

The process can be divided in three parts: (1) 3D machine optimization, (2) materials and post-process treatment and (3) printing parameters optimization.

3.2.3.1 3D machine optimization

It was observed that the ceramic filament, being very brittle, frequently broke. After studying the initial machine configuration, it was found that the filament breakage was due to the extruder configuration, which is designed for polymer materials rather than ceramics. We have dissected the operation of the extruder and organized the possible causes as follows (Figure 22):

1. Filament drive wheel;
2. Nozzle guide;
3. Applied pressure on filament;
4. Temperature increase in the extruder.

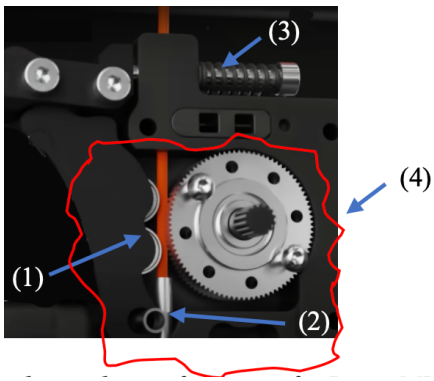

Figure 22: Initial extruder configuration for Prusa MK4

Each problem and its corresponding solution are presented below:

1. In the original configuration, a large gear is positioned on the right side, while two wheels, one above the other, are on the left side (Figure 23). The filament glides between the gear and the wheels. In the case of polymer, this configuration eliminates the inconsistency of volume of extruded plastic when compared to the previous direct drive configuration (two small gears and the filament gliding between them).

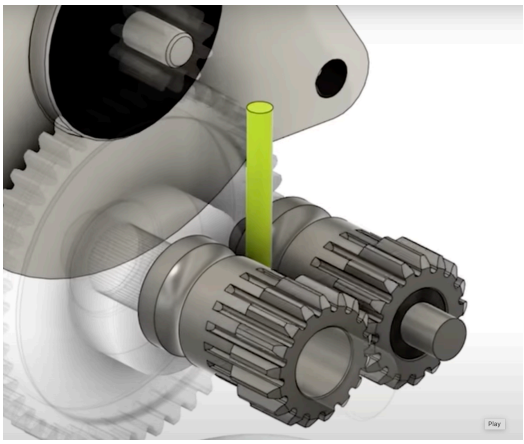

Figure 23: Extruder configuration of models previous to the MK4

But this is not optimal in the case of ceramics (Figure 24).

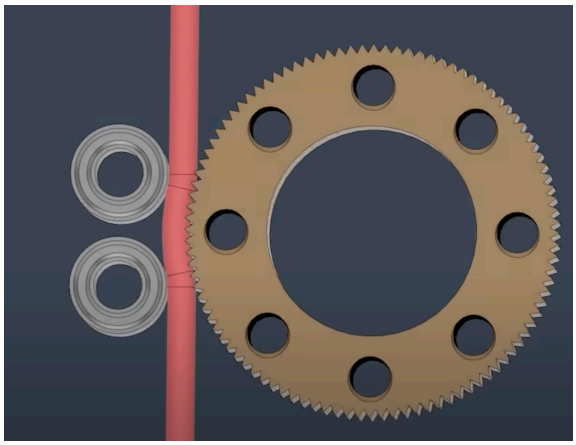

Figure 24: Breakage of the filament due to bending

The slight gap between the two wheels on the left side causes a slight bend in the filament, which, as mentioned earlier, is brittle and it breaks. To solve this problem, the configuration of the extruder was changed so there will be no bending of the filament before reaching the guide, as it is shown in Figure 25.

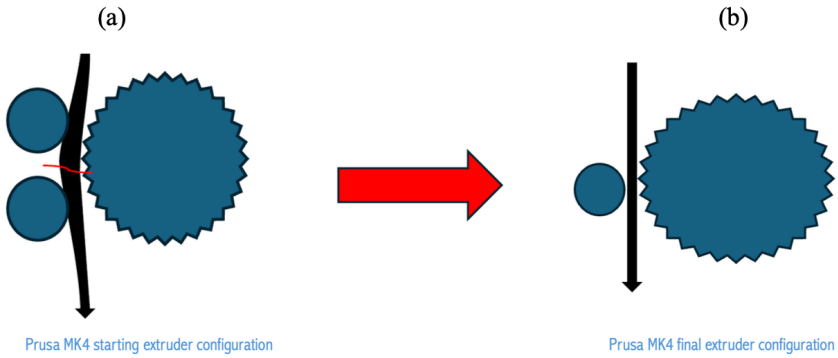

Figure 25: Optimisation of the filament driving wheel

2. In the original configuration, the nozzle guide, meaning the part that leads the filament to the extruder, is made from a hard plastic that does not move. But while printing and the filament is pushed in the extruder, there can be some movement and when the filament meets the plastic part it breaks. To solve that problem, a silicon tube that can follow the movement and deformation of the filament was used. The configuration is presented in Figure 26.

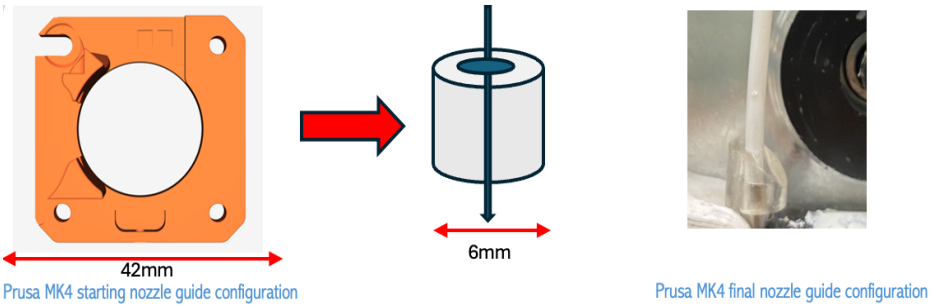

Figure 26: Optimisation of the nozzle guide

3. The next problem that had to be solved was the amount of pressure applied on the filament. In order for the filament to move towards the nozzle, screws and springs can adjust that pressure. By changing the geometry in step 1, the previous installed screws and spring could not provide the right amount of pressure to push the filament without breaking it so larger screws were

installed to increase the distance between the filament and the gear, and hence, decrease the pressure (Figure 27).

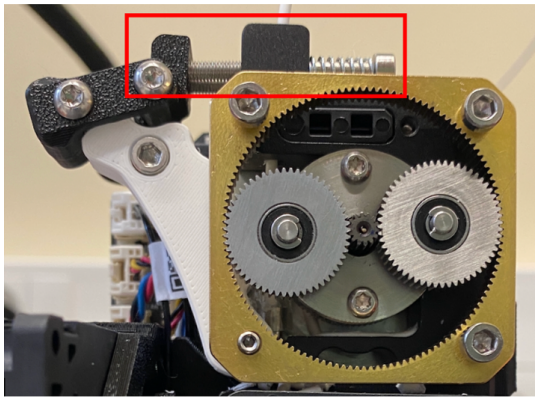

Prusa MK4 applied pressure configuration

Figure 27: Optimisation of the pressure mechanism

4. The last part of configuration is linked to the materials used. When using the Alumina ceramic filament, the recommended printing temperature was 110°C. By putting the filament in a 40°C oven, it was found that its properties change and it becomes very flexible. This flexibility, although is useful because the filament does not break, it is not wanted because it prevents the filament from being pushed in the nozzle. By taking into account the material's temperature sensibility, the front cap of the extruder was removed to assure airflow and temperature stability (Figure 28).

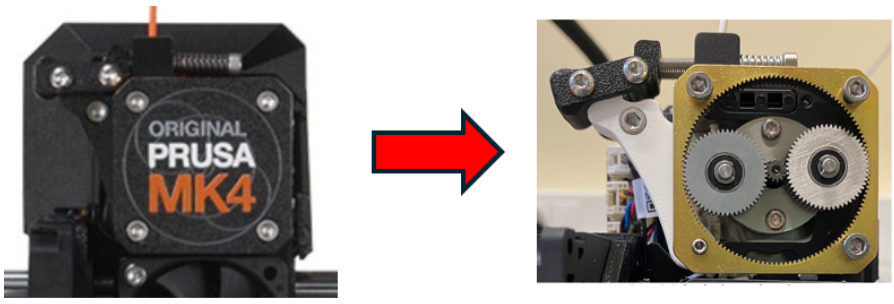

Prusa MK4 original configuration

Prusa MK4 modified configuration

Figure 28: Modification to ensure airflow in the extruder

3.2.3.2 Post-process treatment

After the design and printing of the structure, the obtained part is called the "green part" and post-shaping operations should take place starting with debinding. The debinding step consists of removing the binder from the parts and this must be removed since residues can influence the sintering process and affect the quality of the final product. The most common way to remove the binder from the printed part is by heating it until it melts, flows out and finally degrades. As the binder system in the used filaments includes more than one type of polymer, two-step debinding is required. For this purpose, chemical debinding followed by thermal debinding is performed. During chemical debinding, the part is immersed in acetone that dissolves the support polymer, resulting in the formation of pores in the part. These pores enable the removal of the high-melting-point backbone polymer from the part during thermal debinding. The following and final step is the sintering part which is a thermal treatment that transforms the ceramic powders into bulk materials and is performed at temperature generally within the 70 to 90% of the powder's melting point (Gonzlez-Gutirrez et al., 2012). Before the sintering process, the parts exhibit a highly porous structure comprised of particles with a substantial free surface and elevated surface energy. As heat is applied, the system tends to reduce the surface energy through

the creation of solid bonds between the particles. After the sintering process, shrinkage is observed due to the reduction of the porosity (Gonzalez- Gutierrez et al., 2018; Smirnov et al., 2023). The thermal debinding and sintering stages serve distinct roles but occur sequentially within the same oven as part of a thermal cycle. The debinding protocol and the thermal cycle for each material is presented in Tables 4-5.

Table 4: Debinding and sintering parameters for Alumina

Material	Debinding		Sintering
	Chemical	Thermal	
Alumina	4 hours at acetone bath at 40°C	Up to 500°C with a 8°C /h ramp	20-1550°C with a 50 °C/h and hold for 2 hours

Table 5: Debinding and sintering parameters for Zirconia

Material	Debinding		Sintering
	Chemical	Thermal	
Zirconia	6 hours at acetone bath at 40°C	Up to 500°C with a 8°C /h ramp	20-1475°C with a 50 °C/h and hold for 2 hours

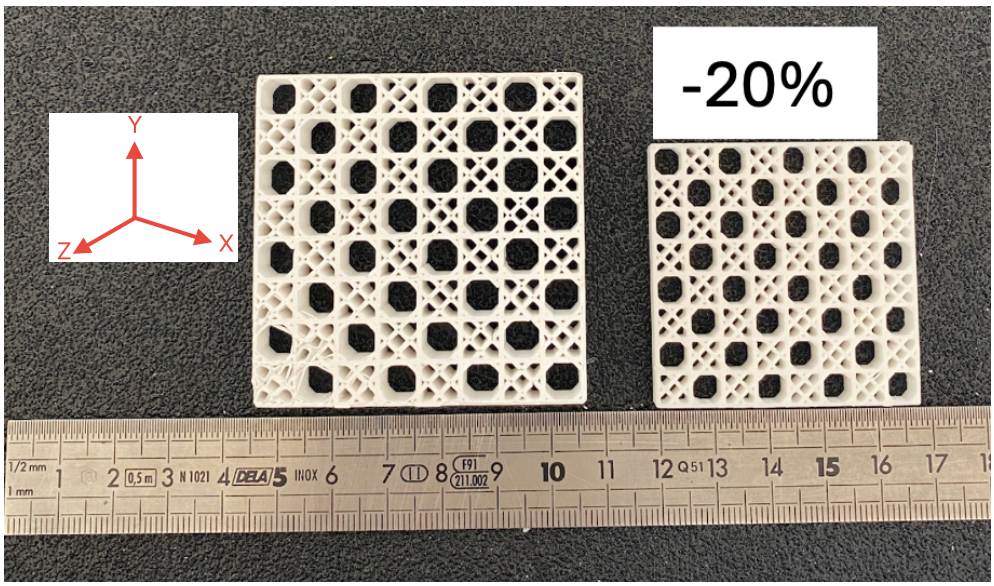

Figure 29: Comparison between green and final zirconia part

The dimensions of each printed sample were measured after sintering and compared to those of "green" samples (Figure 29). The shrinkage was not isotropic, as it was ~ 20% in both X, Y directions and ~ 22% in the Z direction. Note that the total duration to produce a sample is ~ 96 hours (4 days), including the printing, debinding, and sintering times processes.

3.2.3.3 Printing parameters

Commercial printers used for the FFF additive manufacturing method, such as the Prusa MK4, are designed to work with specific materials like PLA, TPU, and other polymers. The use of ceramic materials with this method and these machines is not yet optimized. Therefore, both machine settings

and the slicer software used to prepare models for printing need optimization. The key parameters affecting print quality, and particularly the feasibility of ceramic prints, are printing speed and printing temperature. Various parameters can be adjusted, impacting the final product, but these two are specifically related to the materials used. Although the filament manufacturer suggests values for these parameters, they should be tested and adjusted according to the specifications of different printers.
Once these parameters are optimized and a sample can be printed, other parameters like the retraction speed and the nozzle size, that can affect the surface quality of the sample, are optimized. The surface quality is important for the mechanical testing to ensure a homogenous flat surface. The following images presented in Figures 30-31, produced with a Bruker – DEKTAKX profilometer, show the impact of these parameters on the surface quality. It is worth noting that for different geometries printed, the slicer parameters should be modified.

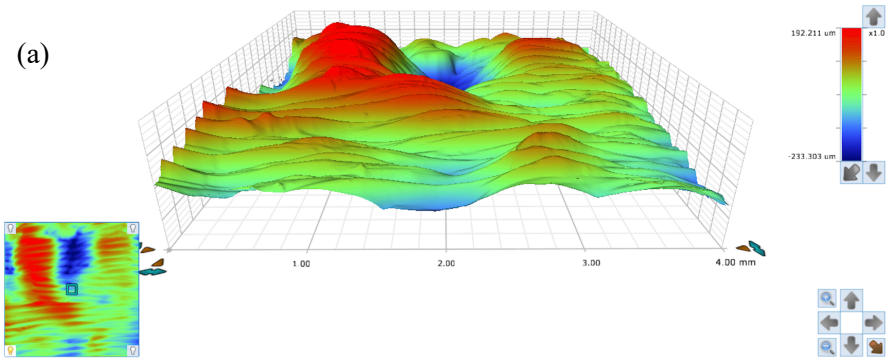

Figure 30: (a) No retraction and nozzle size 0.6 mm - Image produced with Bruker-DEKTAKX profilometer on 4x4 mm sample.

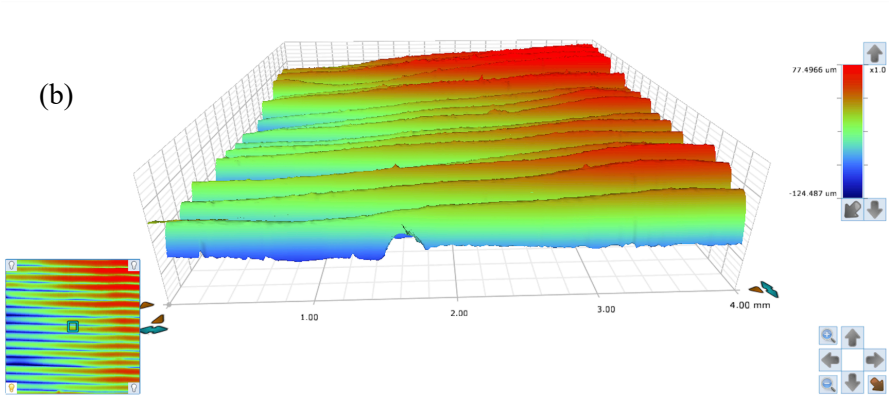

Figure 31: (b) 800 mm/min retraction and nozzle size 0.4 mm – Image produced with Bruker – DEKTAKX profilometer on 4x4 mm sample.

The printing parameters for each material are presented in Tables 6-7.

Table 6: Printing parameters - Alumina

Material	Printing temperatures	Plate temperature	Nozzle size	Layer thickness	Printing speed
Alumina	120 °C (First layer 125°C)	40°C	0.6 mm	0.3mm (first layer 75%)	1200 mm/min (first layer 45%)

Table 7: Printing parameters - Zirconia

Material	Printing temperatures	Plate temperature	Nozzle size	Layer thickness	Printing speed
Zirconia	180 °C	50°C	0.25 - 0.6 mm	0.2mm (first layer 75%)	1200 mm/min (first layer 45%)

3.2.3.4 Compression test of ceramic samples

A compression test was performed on the samples using the Instron 5882, electro-mechanical machine with a maximum load of 100kN at room temperature. The compression tests were conducted under displacement control at 0.1 mm/min. During the test, a CCD camera (pixeLINK®, definition: 2500 x 1600 pixels, digitization: 8 bits) was used to capture the damage of the structure, operating at 1 Hz and equipped with a telecentric objective (GO Edmund, Techspec® gold series, Max distortion: 0.35%, telecentricity: < 0.2°). For this study, six samples were tested with varying relative densities.

Figure 32 shows the values affecting the relative density that are T, D and L, defining the geometry of the structure.

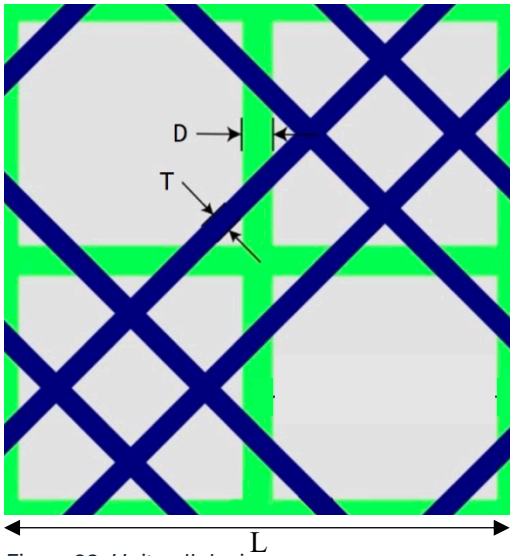

D: thickness of vertical elements
T: thickness of diagonal elements
L: length of unit cell

Figure 32: Unit cell design

To calculate the relative density, the Equation 7 was used.

$$\rho^* = \frac{2[\sqrt{2}\,T(L-2D)+DL-T^2]-D^2}{L^2} \quad (7)$$

The geometry and the relative density of the tested samples is presented in Table 8.

Table 8: Tested samples

Sample	Designed			Printed			ρ*
	t (mm)	d (mm)	L (mm)	t (mm)	d (mm)	L(mm)	
3	0,6	0,9	15	0,75	0,81	11,75	0,28
12	0,6	0,7	10	0,58	0,52	7,7	0,3
10	0,3	0,6	7	0,57	0,59	5,5	0,41

The result of the compression test is a Force (N) – Displacement (mm) graph and by using the geometry of the sample it can be transformed to a Stress (MPa) – Strain (-) curve. The typical response of a ceramic sample under compression test is presented in Figures 33-34.

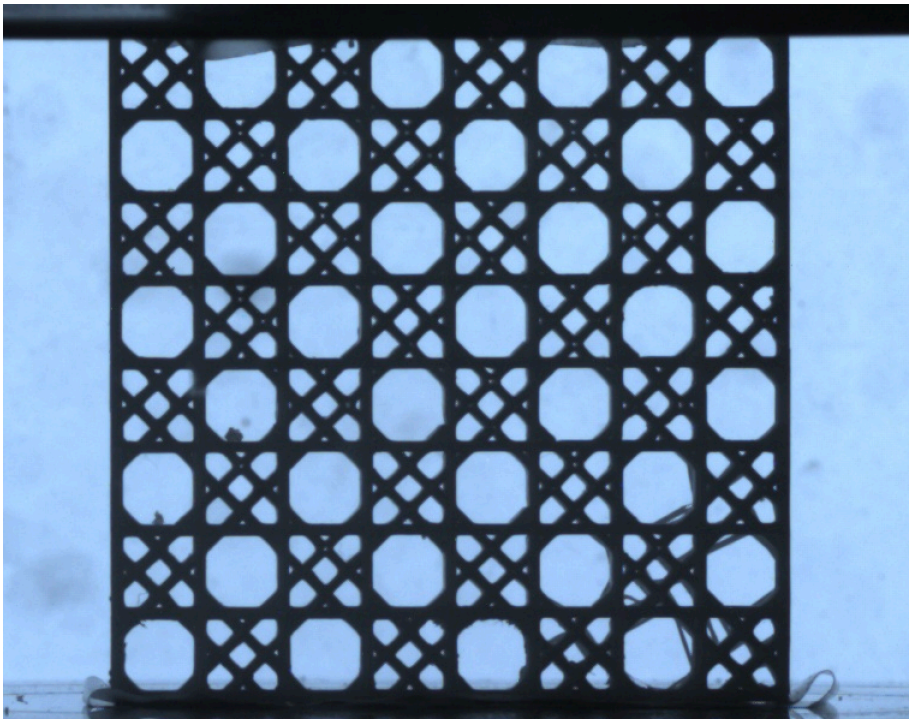

Figure 33: Compression test of a zirconia sample with length of unit cell, L = 15mm.

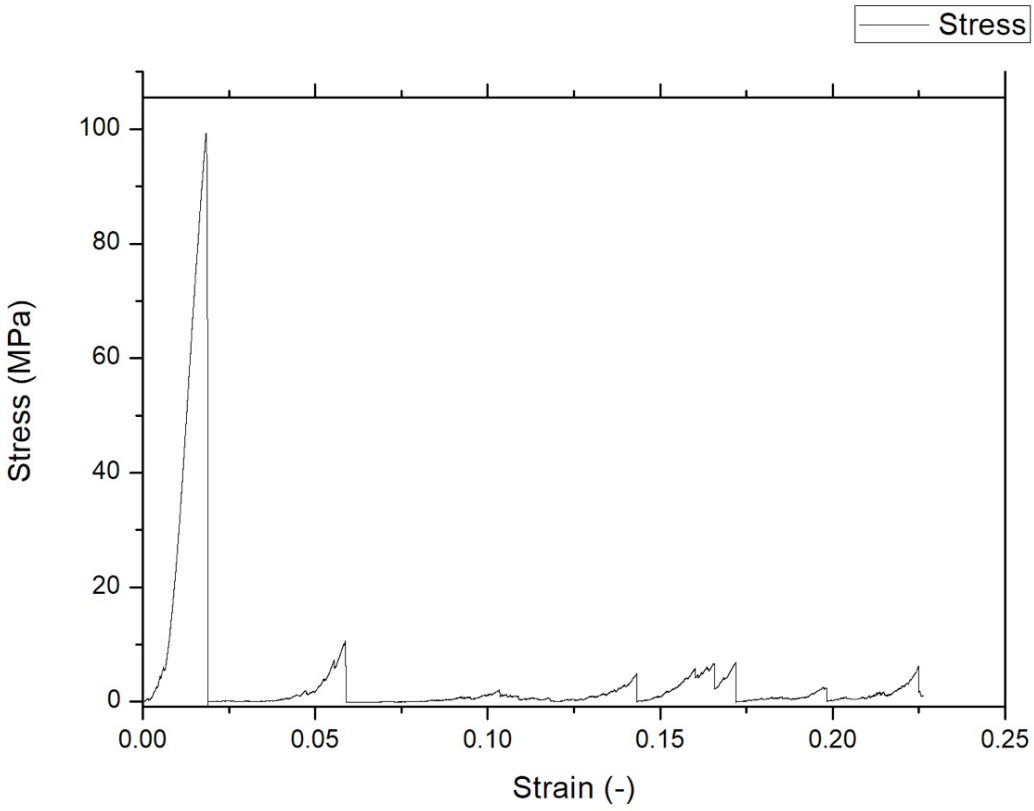

Figure 34: Zirconia sample under compression test – results.

By measuring the area under the curve, the specific energy absorbed by the structure is obtained by Equation 8:

$$SEA\ [J/g] = \frac{1}{\rho_{cell}} \int_0^{\varepsilon_d} \sigma(\varepsilon) d\varepsilon \quad (8)$$

Where:

ε_d is the densification strain,

ρ_{cell} is the density of lattice structure.

3.2.3.5 Compression test of epoxy coated ceramic samples

In order to reduce the fragility of ceramics, we drew inspiration from the internal structure of spicules. As mentioned above, spicules consist of a superposition of multiple cylindrical silica glass separated by a thin layer of protein. This strategy, which is also observed in other species, allows for controlled damage to the ceramic phase and increases its toughness. In order to compare the effect of adding epoxy on the ceramic's compressive mechanical properties, we have made 3 other specimens with the same relative density rate as before. To prepare the samples with the epoxy coating, the following procedure was followed.

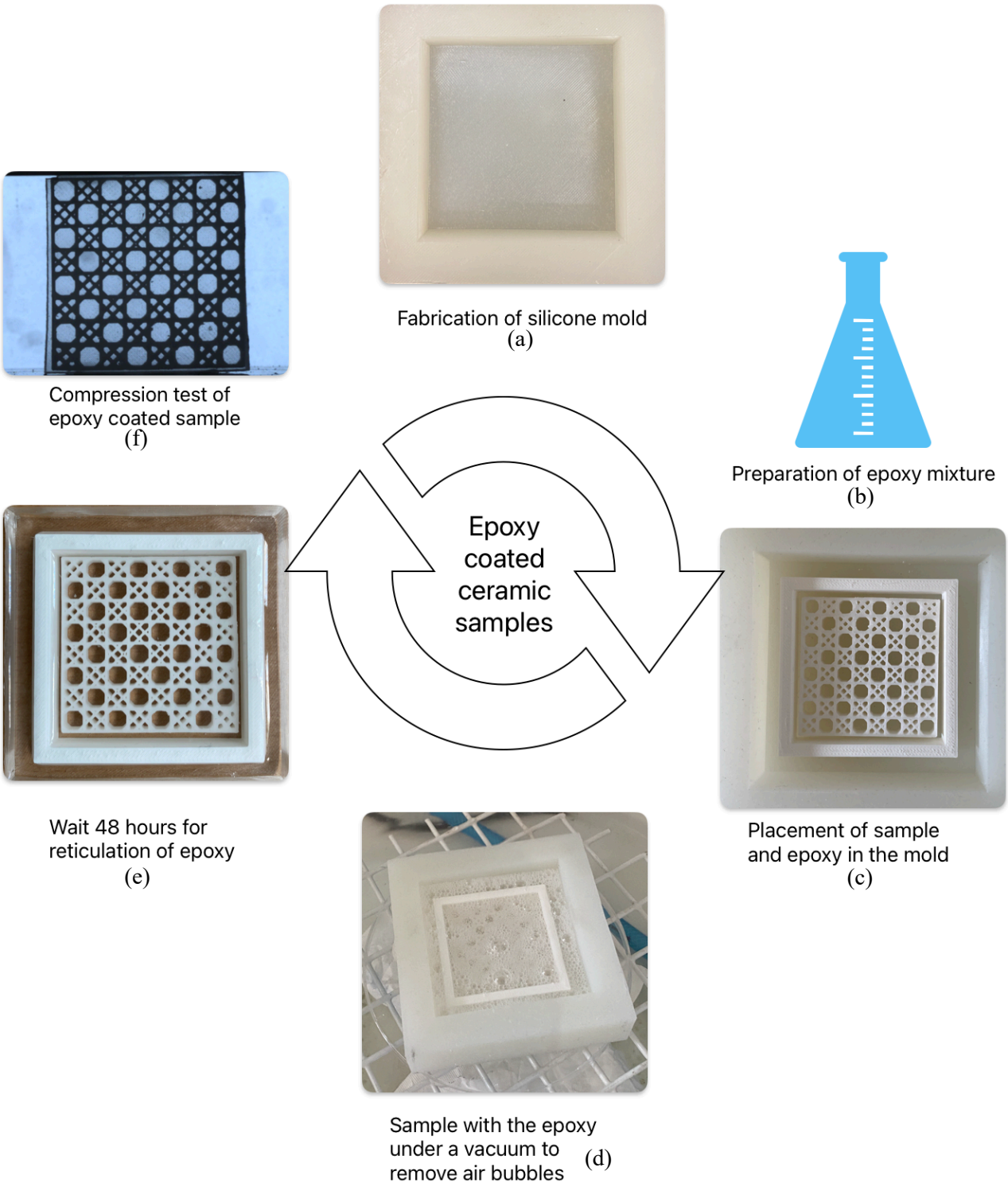

Figure 35: Preparation of epoxy-coated samples

First, a silicone mold was prepared (Figure 35(a)). Silicone was chosen because it allows for easy removal of the epoxy and can be reused multiple times. The epoxy mixture was then prepared according to the manufacturer's instructions, by measuring out 100g resin to 40g hardener before mixing the components and poured into the mold over the ceramic sample (Figure 35(b) and (c)). During the preparation of the mixture and the coating of the sample, air bubbles were trapped in the epoxy. To prevent these air bubbles from affecting the results and to ensure clear images during testing, the sample was then placed in a vacuum chamber to remove the air (Figure 35 (d)) and was set to harden for 48

hours (Figure 35(e)). Finally, the epoxy-coated ceramic sample was tested under compression using the same parameters as for the uncoated one.

3.2.4 Results

For every tested sample, the absorbed energy was calculated from the Stress-Strain curve using equation 8. For the epoxy-coated samples, the same displacement applied to the uncoated samples did not cause any damage to the structure. Therefore, the comparisons in Figures 36-38 are based on different displacements.

While applying compression load on the uncoated ceramic samples, we observed several small cracks that connected and started to propagate through the whole structure with the increasing load, leading to catastrophic failure at a low strain level. The stress vs strain curves is characterized by an initial linear elastic region until fracture. Whereas, the epoxy-coated ceramic samples show the progressive failure.

It is supposed that the crack was initiated by applying a compressive load similar to the uncoated sample; however, the soft polymer coating arrest at the ceramic-polymer interfaces and deflect the crack initiated inside the ceramic. As a result, the whole structure retained continuity. The stress vs strain behavior is characterized by two distinct regimes, as illustrated in figure 38a: (i) an initial linear elastic region until the struts yield due to bending or stretching, (ii) a roughly constant stress plateau region, corresponding to cell collapse by buckling and fracture.

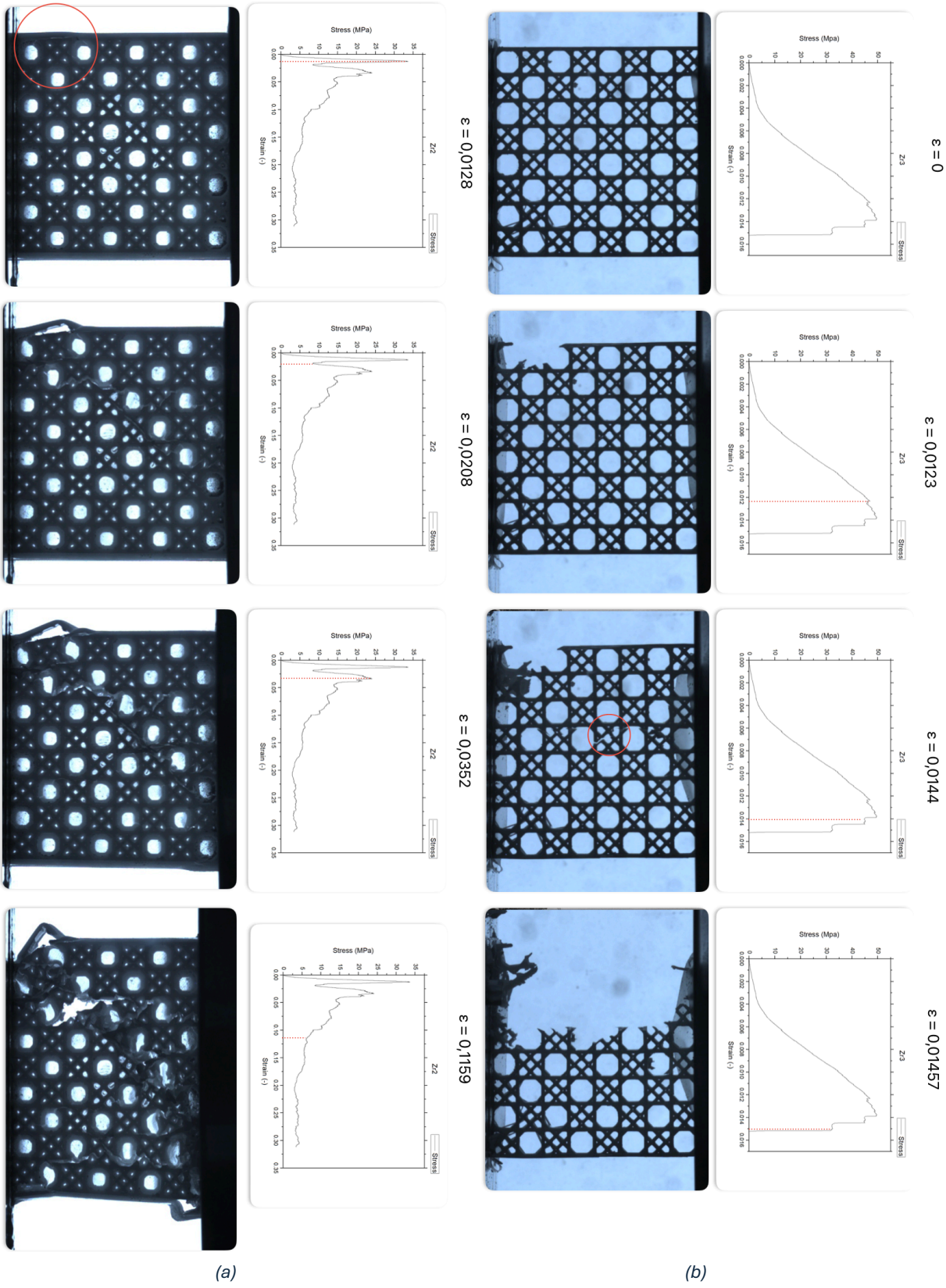

Figure 36: Compression results with a series of snapshots from compressive tests of (a) epoxy-coated Zirconia samples (Zr2) and (b) uncoated ones (Zr3),Relative density = 0.27, Zr3: SEA = 0.206 J/g, Zr2: SEA =1.51 J/g

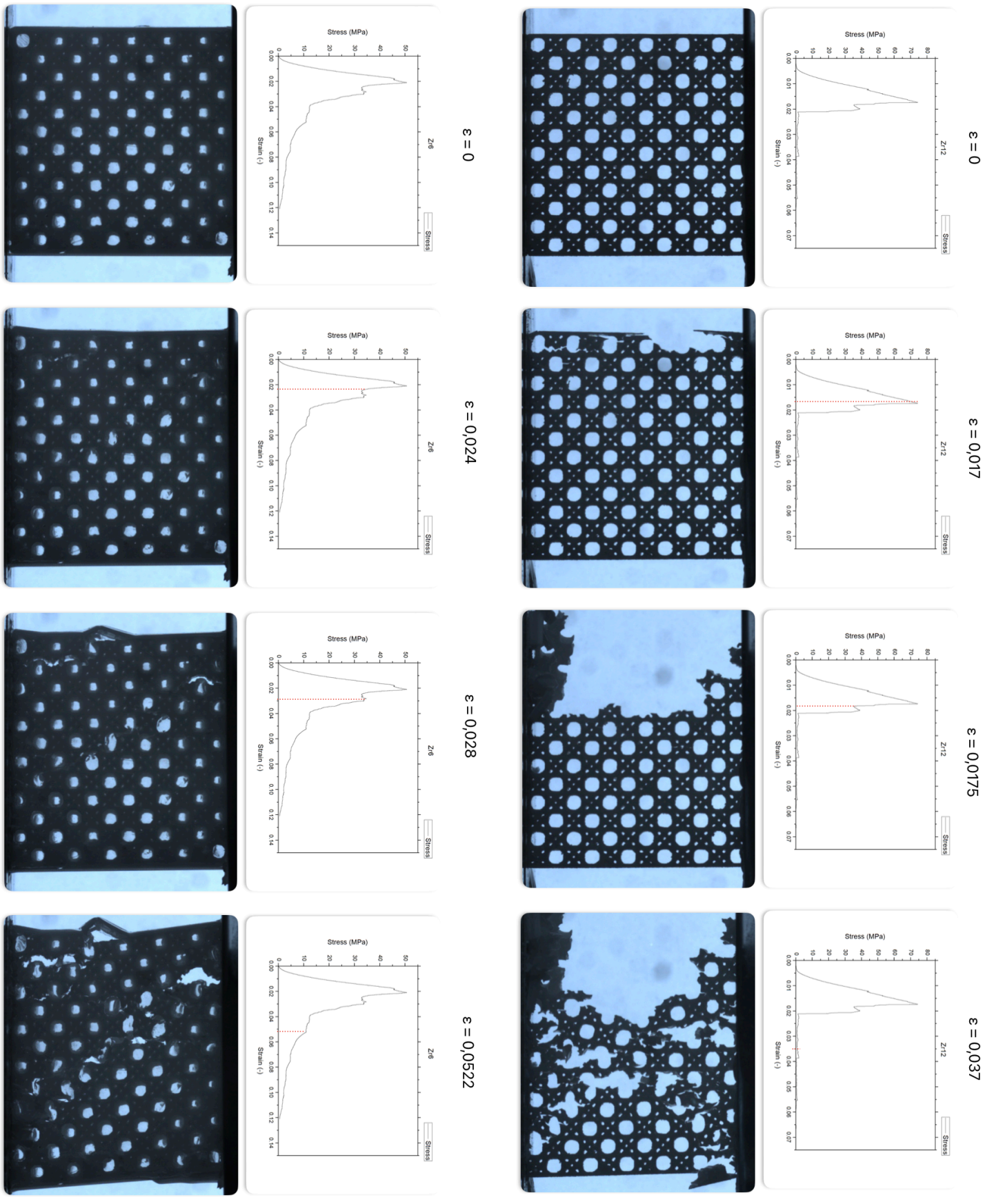

Figure 37: Compression results with a series of snapshots from compressive tests of (a) epoxy-coated Zirconia samples (Zr6) and (b) uncoated ones (Zr12), Relative density = 0.30, Zr12: SEA = 0.109 J/g, Zr6: SEA =0.228 J/g

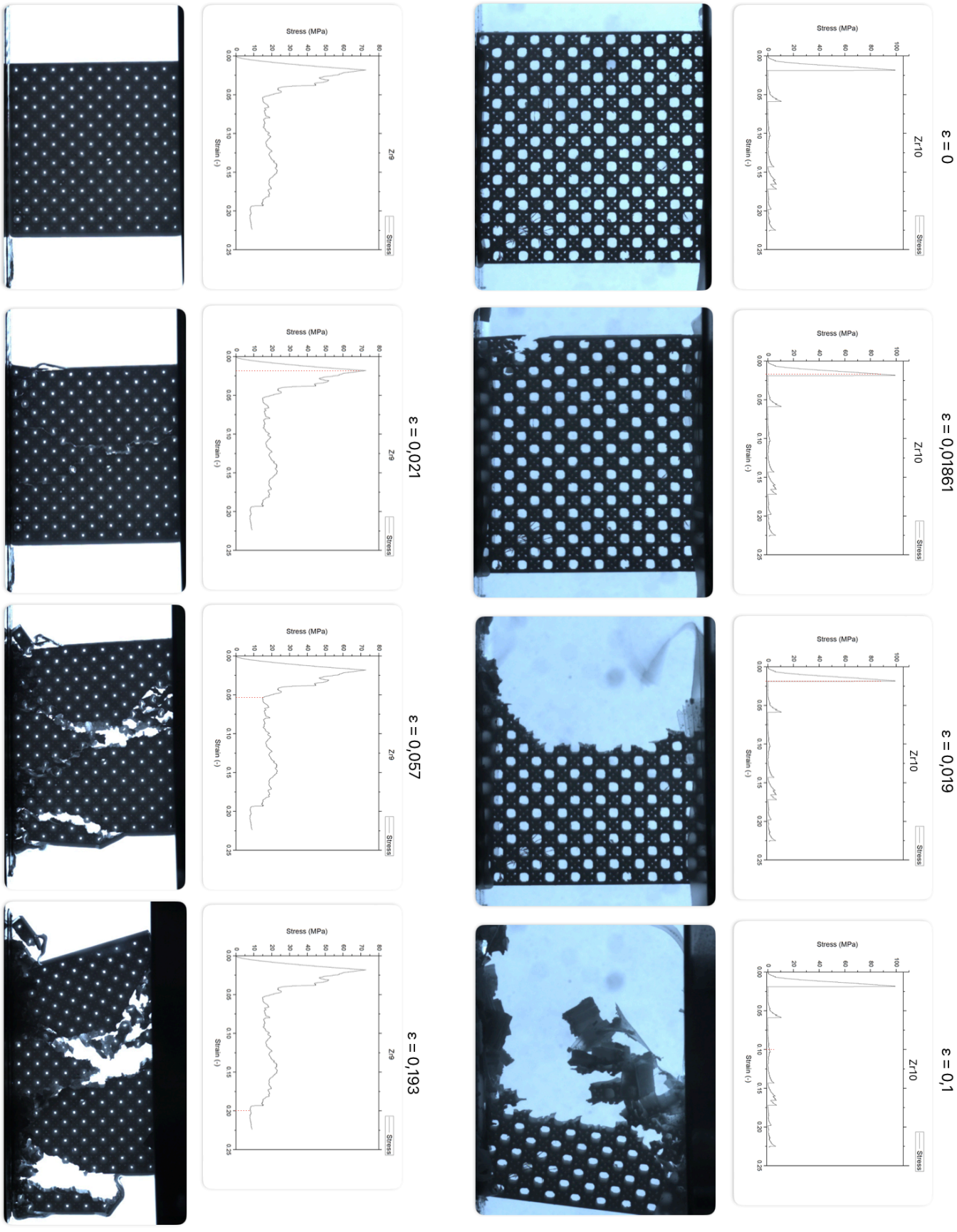

Figure 38: Compression results with a series of snapshots from compressive tests of (a) epoxy-coated Zirconia samples (Zr9) and (b) uncoated ones (Zr10), Relative density = 0.41, Zr10: SEA = 0.389 J/g, Zr9: SEA =2.51 J/g

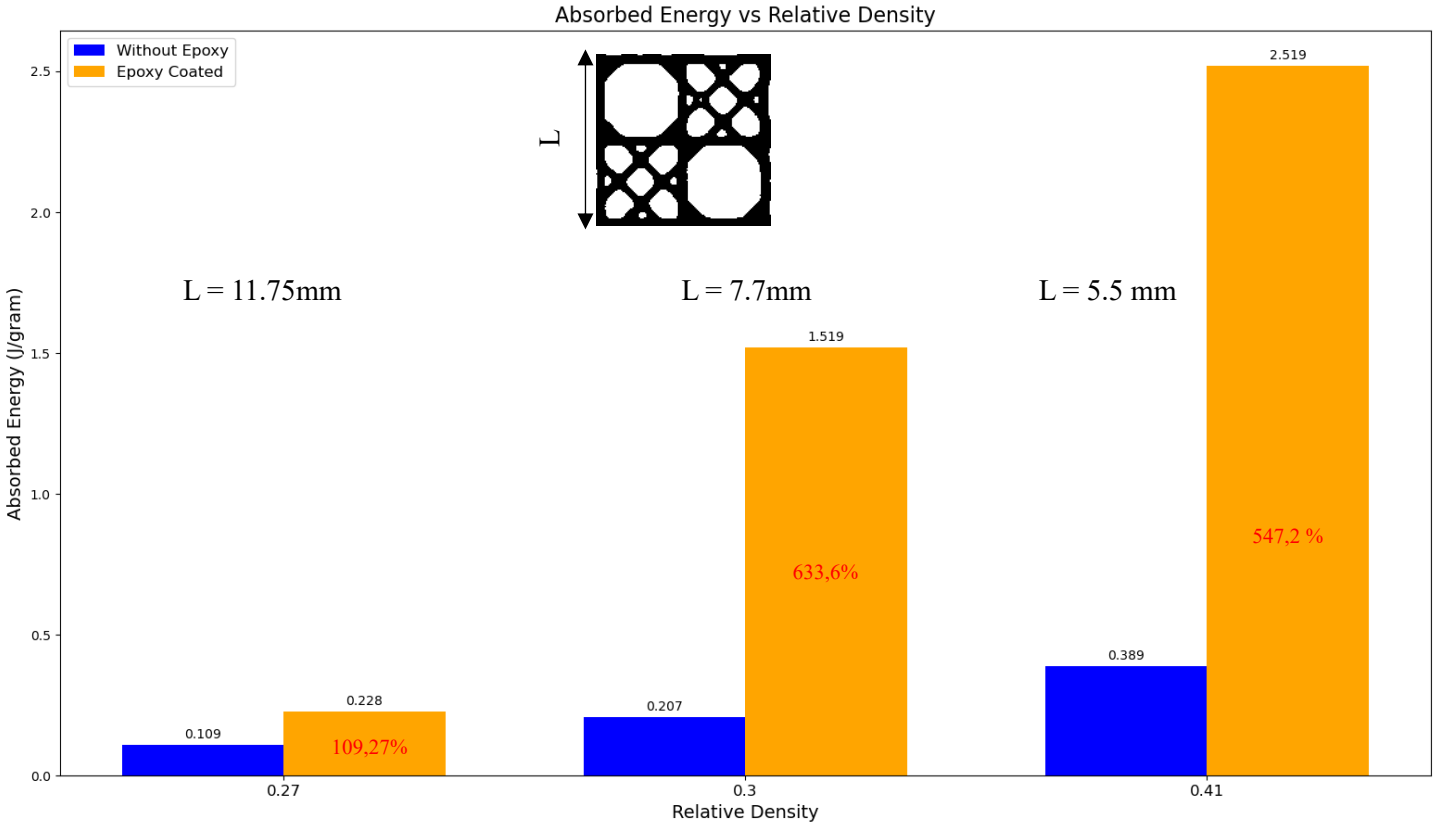

Figure 39: Energy absorption capability.

As presented in the figure 39, samples with higher relative density have higher energy absorption. For the samples with the same relative density, the ones with the epoxy coating absorbed significant more energy when compared to the uncoated ones. In Table 9 the amount of epoxy added to the samples is presented.

Table 9: Epoxy % added to samples.

Before epoxy (grams)	After epoxy (grams)	Epoxy %
46.657	59.558	27.62%
58.126	67.87	16.76%
71.65	81.627	13.93%

4. Conclusion

The results of this study enhance our understanding of the sponge's structure on a multi-scale level and reaffirm the principle of bio-inspiration: nature knows the best. The examination of the microstructure reveals the complexity of the sponge's building blocks, the spicules, enabling us to compile a comprehensive database of their characteristics, including composition and mechanical behavior. Our findings on the mechanical properties of spicules corroborates the data in current scientific literature but were achieved through a simpler and more cost-effective method, providing an opportunity for further extensive testing and deeper research. The study of the mesostructure achieved multiple objectives. Firstly, the optimization of the FFF additive manufacturing method using ceramic materials enabled the production of samples with remarkable detail, surpassing previous efforts in this field. This method successfully replicated a bio-inspired structure with ceramic materials, a unique achievement to the author's knowledge. The study demonstrates a successfully 3D-printed bio-inspired EA sponge

structures using alumina (Al_2O_3) and zirconia (ZrO_2) using FFF process with relative densities ranging from 0.28 to 0.41. With, in some cases, cell sizes identical to those found in natural sponges (L=5 mm). Given the inherent fragility and limited toughness of ceramics, our approach draws inspiration from sponge spicules that create a multilayered material using silica glass (as the rigid component) separated by a protein-based material (the soft component). To achieve this, we coated ceramic samples with a thin layer of epoxy and compared energy absorption during compression tests with uncoated ceramic structures. Preliminary results indicate that the polymer coating enhances compressive strength and increases specific energy absorption by a factor of ~ 6. Further analysis of the test results is ongoing. This study provided the opportunity to engage with various subjects, ranging from software and machine optimization to the development of mold and epoxy protocols. These experiences have equipped me with the resources to further pursue research in this field and knowledge that will be invaluable in advancing my professional career.

5. References

1. Ashby, M.F., 2006. The properties of foams and lattices. Phil. Trans. R. Soc. A. 364, 15–30. https://doi.org/10.1098/rsta.2005.1678

2. Ashby M.F., Gibson I.J. (1982). The mechanics of three-dimensional cellular materials. Proc. R. Soc. A., 382(1782), 43–59.

3. Bar-Cohen, Y., Biomimetics: biologically inspired technology.

4. Benedetti M., du Plessis A., Ritchie R.O., Dallago M., Razavi N., 2021. Berto F., Architected cellular materials: A review on their mechanical properties towards fatigue-tolerant design and fabrication. Materials Science & Engineering R 144, 100606. https://doi.org/10.1016/j.mser.2021.100606

5. Bergeret A., Krawczak P. (2006). Liaison renfort/matrice : Définition et caractérisation. Plastique et Composites. Tech. L'ingénieur, no. N° AM5305.

6. Braun T., Diot C., Hoglander A., ROCA V. (1995). An experimental user level implementation of TCP. Rapport de recherche n° 265, INRIA, septembre 1995.

7. Boufaida. (2015). Analyse des propriétés mécaniques de composites taffetas verre/matrice acrylique en relation avec les propriétés d'adhésion des fibres sur la matrice.

8. Cano, S., Gonzalez-Gutierrez, J., Sapkota, J., Spoerk, M., Arbeiter, F., Schuschnigg, S., Holzer, C., Kukla, C., 2019. Additive manufacturing of zirconia parts by fused filament fabrication and solvent debinding: Selection of binder formulation. Additive Manufacturing 26, 117–128. https://doi.org/10.1016/j.addma.2019.01.001

9. Deshpande, V.S., Ashby, M.F., Fleck, N.A., 2001. Foam topology: bending versus stretching dominated architectures. Acta Materialia 49, 1035–1040. https://doi.org/10.1016/S1359-6454(00)00379-7

10. Dunlop, J.W.C., Weinkamer, R., Fratzl, P., 2011. Artful interfaces within biological materials. Materials Today 14, 70–78. https://doi.org/10.1016/S1369-7021(11)70056-6

11. Feillard P., Désarmot G., Favre J.P. (1993). A critical assessment of the fragmentation test for glass/epoxy systems. Compos. Sci. Technol., 49(2), 109–119.

12. Fernandes, M.C., Aizenberg, J., Weaver, J.C., Bertoldi, K., 2021. Mechanically robust lattices inspired by deep-sea glass sponges. Nat. Mater. 20, 237–241. https://doi.org/10.1038/s41563-020-0798-1

13. Fischer S.F., Thielen M., Loprang R.R., Seidel R., Fleck C., Speck T., et al. (2010). Pummelos as Concept Generators for Biomimetically Inspired Low Weight Structures with Excellent Damping Properties. Adv Eng Mater., 12(12), B658-B63.

14. Gibson, L. J., & Ashby, M. F. (1999). Cellular solids: structure and properties. Cambridge university press.

15. Gibson I.J., Ashby M.F. (1982). The mechanics of three-dimensional cellular materials. Proc. R. Soc. A., 382(1782), 43–59.

16. Gonzalez-Gutierrez J., Cano S., Schuschnigg S., Kukla C., Sapkota J., Holzer C. (2018). Additive Manufacturing of Metallic and Ceramic Components by the Material Extrusion of Highly-Filled Polymers: A Review and Future Perspectives. Materials, 11, 840. https://doi.org/10.3390/ma11050840

17. Gonzalez-Gutierrez J., Stringari G., Emri I. (2012). Powder Injection Molding of Metal and Ceramic Parts. In Wang J. (Ed.), *Some Critical Issues for Injection Molding (pp. 65–86).

18. Ha N.S., Lu G. (2020). A review of recent research on bio-inspired structures and materials for energy absorption applications. Composites Part B: Engineering, 181, 107496. https://doi.org/10.1016/j.compositesb.2019.107496

19. Harris M., Potgieter J., Archer R., Arif K.M. (2019). Effect of Material and Process Specific Factors on the Strength of Printed Parts in Fused Filament Fabrication: A Review of Recent Developments. Materials, 12, 1664.

20. Herrera-Franco P (2005). Fiber-Matrix Adhesion in Natural Fiber Composites.

21. Le Duigou A., Barbé A., Guillou E., Castro M. (2019). 3D printing of continuous flax fibre reinforced biocomposites for structural applications. Mater & Des., 180, 107884.

22. Le Duigou A., Correa D., Ueda M., Matsuzaki R., Castro M. (2020). A Review of 3D and 4D Printing of Natural Fibre Biocomposites. Mater. Des., 194, 108911.

23. Li QM, Magkiriadis I, Harrigan JJ. Compressive Strain at the Onset of Densification of Cellular Solids. Journal of Cellular Plastics. 2006;42(5):371-392. doi:10.1177/0021955X06063519

24. Maconachie M., Leary B., Lozanovski X., Zhang M., Qian O., Faruque M., Brandt S. (2019). SLM lattice structures: properties, performance, applications and challenges. Mater. Des., 183, 108137. https://doi.org/10.1016/j.matdes.2019.108137

25. Matsuzaki R., Ueda M., Namiki M., Jeong T.K., Asahara H., Horiguchi K., Nakamura T., Todoroki A., Hirano Y. (2016). Three-dimensional printing of continuous-fiber composites by in-nozzle impregnation. *Sci. Rep.*, 6, 23058.

26. Miserez, A., Weaver, J.C., Thurner, P.J., Aizenberg, J., Dauphin, Y., Fratzl, P., Morse, D.E. and Zok, F.W. (2008), Effects of Laminate Architecture on Fracture Resistance of Sponge Biosilica: Lessons from Nature†. Adv. Funct. Mater., 18: 1241-1248. https://doi.org/10.1002/adfm.200701135

27. Nanoe (2020). Zetamix 3D printing filament. Available at: https://zetamix.fr/en/produit/zetamix-alumina-filament.

28. Orlovska M., Chlup Z., Baca L., Janek M., Kitzmantel M. (2020). Fracture and mechanical properties of lightweight alumina ceramics prepared by fused filament fabrication. J. Eur. Ceram. Soc., 40, 4837–4843. https://doi.org/10.1016/j.jeurceramsoc.2020.02.026

29. Pokroy, B., Demensky, V., Zolotoyabko, E., 2009. Nacre in Mollusk Shells as a Multilayered Structure with Strain Gradient. Adv Funct Materials 19, 1054–1059. https://doi.org/10.1002/adfm.200801201

30. Ramazani H., Kami A. Metal FDM, a new extrusion-based additive manufacturing technology for manufacturing of metallic parts: a review. *Prog Addit Manuf* **7**, 609–626 (2022). https://doi.org/10.1007/s40964-021-00250-x

31. Somera, A., Poncelet, M., Auffray, N., Réthoré, J., 2022. Quasi-periodic lattices: Pattern matters too. Scripta Materialia 209, 114378. https://doi.org/10.1016/j.scriptamat.2021.114378

32. Sun Y., Yu Z., Wang Z., Liu X. (2015). Novel protective covering to enhance concrete resistance against projectile impact. Construction and Building Materials, 96, 484-490.

33. Tao W., Leu M.C. (2016). Design of lattice structure for additive manufacturing. 2016 International Symposium on Flexible Automation (ISFA), IEEE, pp. 325–332. https://doi.org/10.1109/ISFA.2016.7790182

34. Virtual Foundry (2023). Ceramic Filaments. Available at: https://shop.thevirtualfoundry.com/collections/ceramic-filaments. Accessed 11 Jan 2023.

35. Weaver JC, Aizenberg J, Fantner GE, Kisailus D, Woesz A, Allen P, Fields K, Porter MJ, Zok FW, Hansma PK, Fratzl P, Morse DE. Hierarchical assembly of the siliceous skeletal lattice of the hexactinellid sponge Euplectella aspergillum. J Struct Biol. 2007 Apr;158(1):93-106. doi: 10.1016/j.jsb.2006.10.027. Epub 2006 Nov 10. PMID: 17175169.

36. Woesz, A., Weaver, J.C., Kazanci, M., Dauphin, Y., Aizenberg, J., Morse, D.E., Fratzl, P., 2006. Micromechanical properties of biological silica in skeletons of deep-sea sponges. J. Mater. Res. 21, 2068–2078. https://doi.org/10.1557/jmr.2006.0251

37. Yang C., Tian X., Liu T., Cao Y., Li D. (2017). 3D printing for continuous fiber reinforced thermoplastic composites: Mechanism and performance. Rapid Prototyp. J., 23, 209–215.

38. Zhong, H., Song, T., Li, C., Das, R., Gu, J., Qian, M., 2023. The Gibson-Ashby model for additively manufactured metal lattice materials: Its theoretical basis, limitations and new insights from remedies. Current Opinion in Solid State and Materials Science 27, 101081. https://doi.org/10.1016/j.cossms.2023.101081

6. Supplementary material

Supplementary Table 1

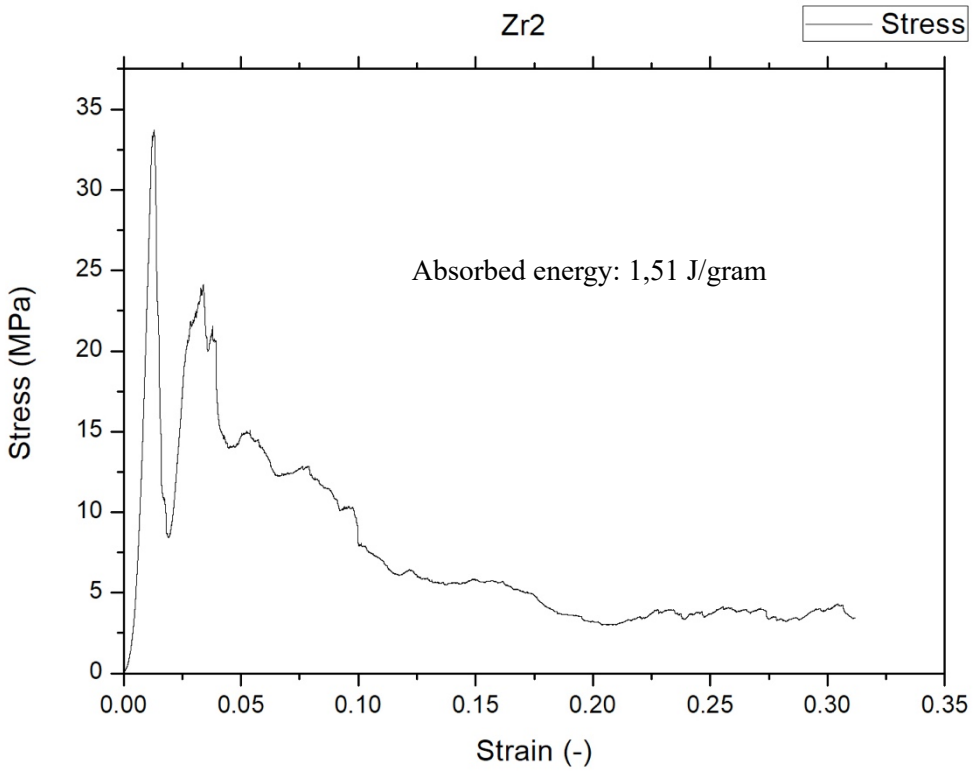

Supplementary Table 2

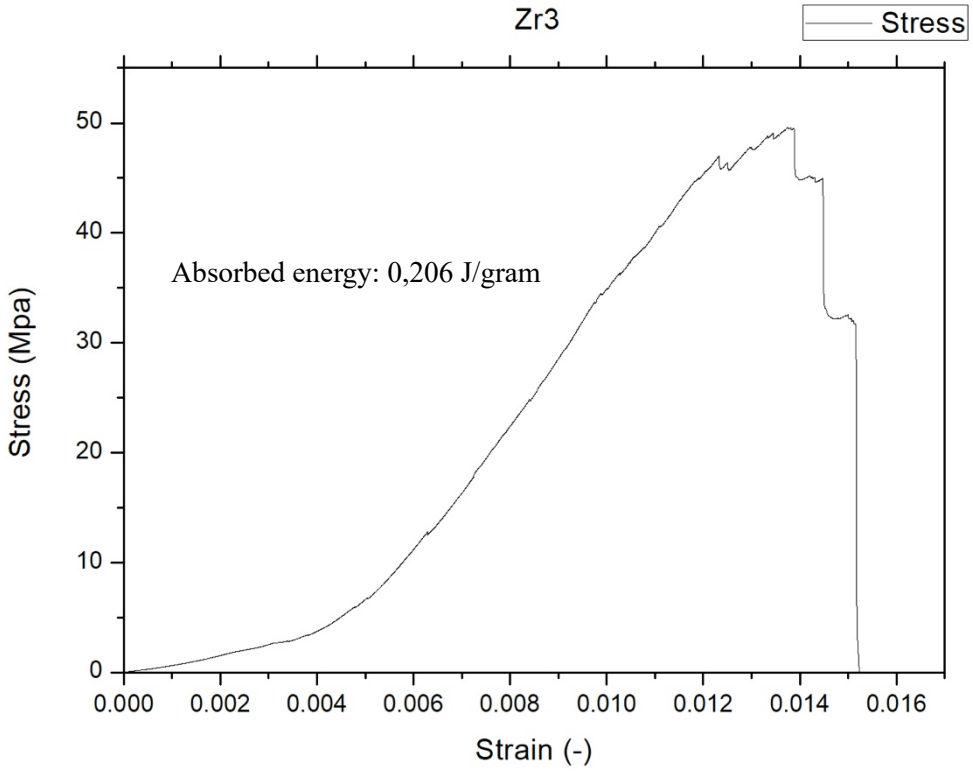

Supplementary Table 3

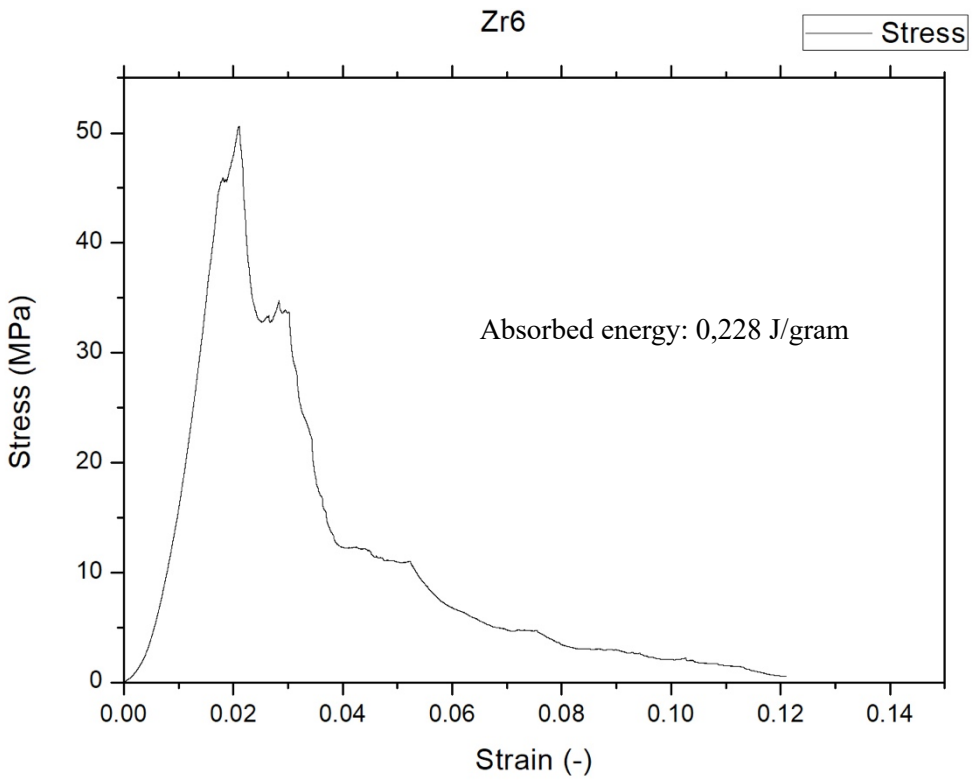

Supplementary Table 4

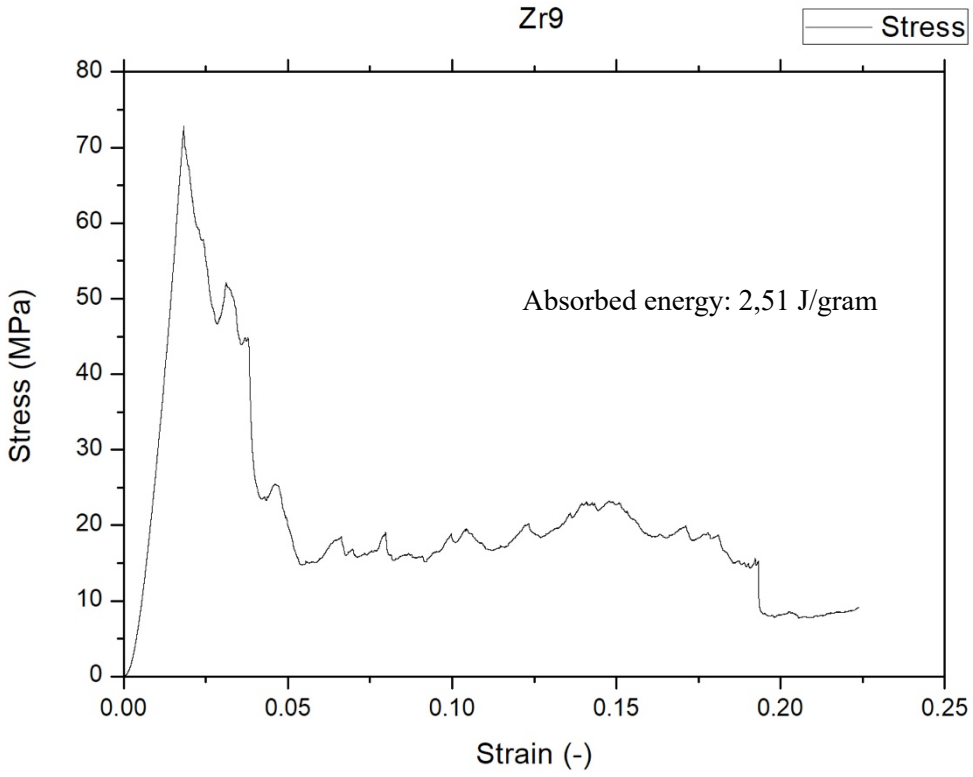

Supplementary Table 5

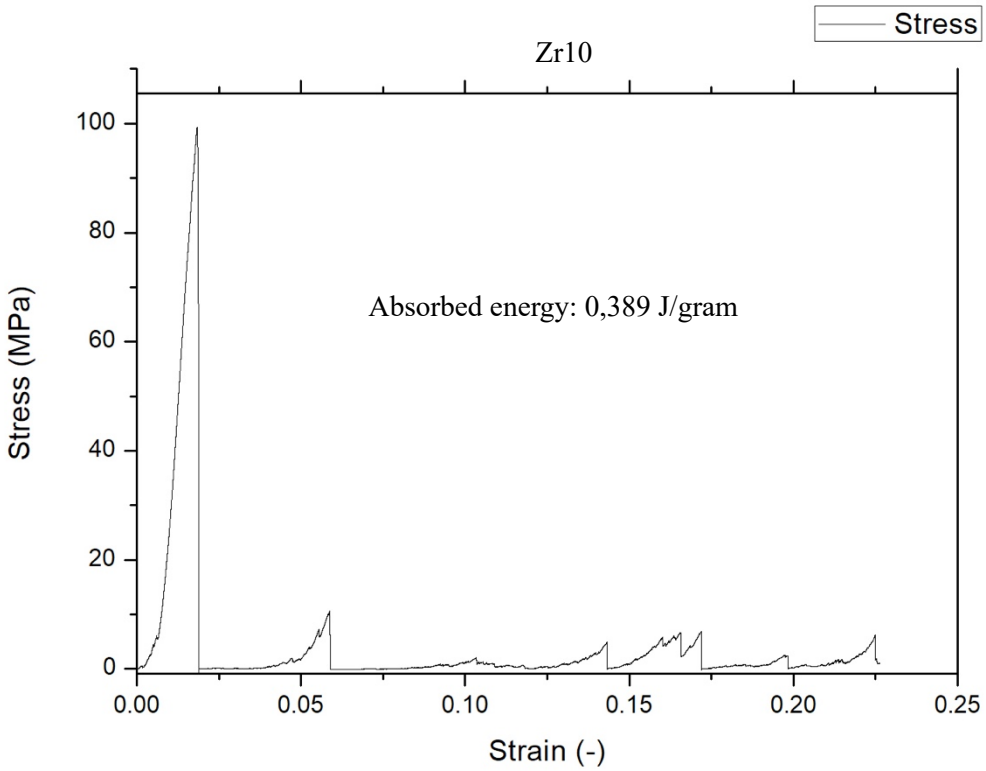

Supplementary Table 6